



**Abstract**

The active deformation field in subduction forearcs provides critical information about the stress and strain state of the upper plate and its potential for seismogenesis. However, these properties are challenging to quantify in most subduction systems, and in the northern Cascadia forearc, few faults have been identified that can be used to reconstruct the upper plate deformation field. Here we investigate the slip history of the Beaufort Range fault (BRF) on Vancouver Island. This fault was proposed to host the 1946  $M_{7.3}$  Vancouver Island earthquake, but no surface rupture or evidence of Quaternary activity has been documented, and the stress and strain conditions that promoted this event are poorly understood. We provide the first evidence that the BRF is active, using newly-collected lidar to map topographic scarps along the fault system and to reconstruct slip vectors from offset geomorphic markers. Quaternary deposits and landforms that show increasing magnitude of displacement with age provide evidence for at least three  $M_W \sim 6.5-7.5$  earthquakes since  $\sim 15$  ka, with the most recent event occurring  $< 3-4$  ka. Kinematic inversions of offset geomorphic markers show that the BRF accommodates right-lateral transtension along a steeply NE-dipping fault. This fault geometry and kinematics are similar to those modeled for the 1946 earthquake, suggesting that the BRF is a candidate source fault for this event. We find that the kinematics of the BRF are consistent over decadal to millennial timescales, suggesting that this portion of the northern Cascadia forearc has accommodated transtension over multiple earthquake cycles.

**Plain Language Summary**

Subduction zones, like Cascadia, contain onshore fault networks that can host earthquakes that are dangerous to communities. However in many locations, like Vancouver Island, Canada, we know little about where these faults are and what type and magnitude earthquake they can host (if any). We focus on the Beaufort Range fault (BRF) on Vancouver Island, and show for the first time that the BRF hosted recent earthquakes. Newly-available high-resolution topography data show many scarps, or vertical offsets of the ground surface produced in past earthquakes, along a  $> 40$  km zone. Surveys of landforms that have been offset by the BRF show both vertical and horizontal offsets along a near-vertical fault. The nearby 1946 Vancouver Island earthquake had similar vertical and horizontal offsets along a near-vertical fault, suggesting that this earthquake might have happened on the BRF. Our data show there have been  $> 3$  large earthquakes

52 on the BRF in the past  $\sim 15,000$  years, the most recent  $< 3,000$ - $4,000$  years ago. The off-  
53 sets we observe suggest these earthquakes had magnitudes between  $\sim 6.5$  and  $7.5$ . Fu-  
54 ture similar earthquakes could cause shaking damage to many nearby communities, in-  
55 cluding the cities of Port Alberni and Nanaimo, and nearby hydroelectric facilities.

## 56 1 Introduction

57 Quantifying the stress state and strain history of subduction zone forearcs is crit-  
58 ical for understanding the energy budget of convergent margins (e.g., Huang et al., 2022),  
59 the seismic potential and hazard of forearc faults (e.g., Wang et al., 1995; Balfour et al.,  
60 2011; Thenhaus & Campbell, 2002), and the evolution of the upper plate during the megath-  
61 rust seismic cycle (e.g., Regalla et al., 2017; Herman & Govers, 2020). However, stress  
62 is notoriously difficult to measure or approximate, and in the northern Cascadia fore-  
63 arc of Vancouver Island, there are several competing models for what controls forearc  
64 stress and upper plate deformation (e.g., Mazzotti et al., 2011; Finley et al., 2019; De-  
65 lano et al., 2017). Quantifying upper plate deformation is also limited in Cascadia be-  
66 cause the subduction zone is relatively seismically quiet, limiting our ability to infer stress  
67 field data from seismicity. Furthermore, the large locking signal on the plate interface  
68 inhibits our ability to isolate Global Navigation Satellite System (GNSS) deformation  
69 associated with upper plate faults (e.g., Mazzotti et al., 2011; S. Li et al., 2018), and few  
70 active upper plate faults have been identified regionally to date (e.g., Morell et al., 2017).

71 Although the northern Cascadia region exhibits relatively low rates of instrumen-  
72 tal seismicity, this region was also host to the largest onshore historic earthquake in Canada,  
73 the M 7.3 1946 Vancouver Island earthquake (Rogers & Hasegawa, 1978; Rogers, 1979;  
74 Lamontagne et al., 2018). This earthquake is the largest to have occurred anywhere within  
75 the Cascadia subduction zone system, including the megathrust, since written histor-  
76 ical recordkeeping began (the past  $\sim 200$  yrs). However, despite this earthquake's size  
77 and moderate damage to nearby population centers (Hodgson, 1946; Mathews, 1979; Clague,  
78 1996), the fault that ruptured during the 1946 earthquake remains unknown. In addi-  
79 tion, little is known about the current or past stress state and strain field of the crust  
80 surrounding this major historical rupture, what upper plate conditions could lead to fu-  
81 ture ruptures, and if similar events have occurred in the geologic past. Such data are nec-  
82 essary not only to evaluate the seismic potential of forearc faults, but also to determine  
83 their deformation rates, kinematics, and relationship to the regional stress field. Yet, no

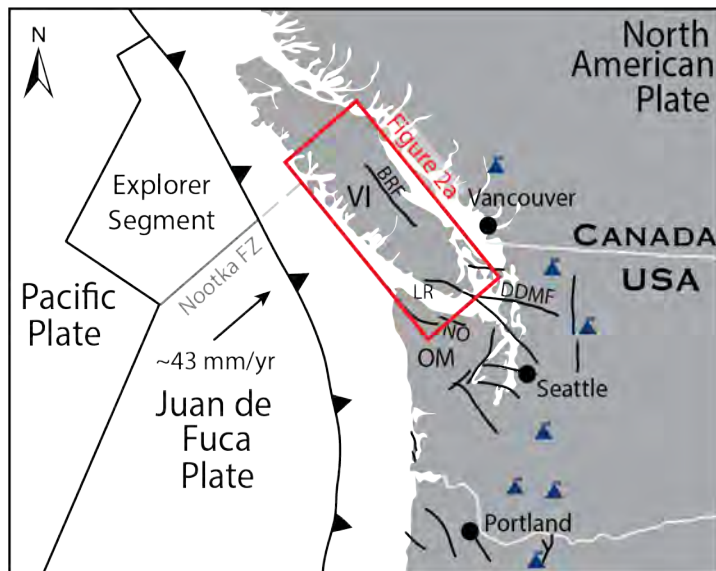


**Figure 1.** Regional tectonic setting showing the location of the Beaufort Range fault (BRF) and other active faults in the Cascadia forearc of Canada and the USA. Juan de Fuca – North America convergence vector after Kreemer et al. (2014). Slab depth contours from Slab2 (Hayes et al., 2018). Active faults in USA after USGS (Geological Survey, n.d.), Leech River fault after Morell et al. (2017), volcanoes after AGI (2003). Red box shows location of Figure 2a. DDMF – Darrington-Deviils Mountain fault; FZ — fault zone; LR – Leech River fault; NO - North Olympic fault zone; OM - Olympic Mountains; VI - Vancouver Island.

84 active faults have been identified north of the greater Victoria region to date, including  
 85 in the region surrounding the approximate epicenter of the 1946 earthquake.

86 Here, we investigate the kinematics and slip history of the Beaufort Range Fault  
 87 (BRF), a major fault in the northern Cascadia forearc, to evaluate how forearc strain  
 88 is accommodated on this structure over decadal to millennial timescales. The BRF is  
 89 located on central Vancouver Island, near the northern terminus of the Cascadia sub-  
 90 duction zone (Figure 1). Several researchers proposed that the Beaufort Range fault may  
 91 have hosted the 1946 rupture, based on the proximity of the epicenter, coseismic slip mod-  
 92 eled from geodetic benchmark surveys, and the similarity of the BRF strike to the NW-  
 93 SE striking nodal plane for the event’s focal mechanism (Rogers & Hasegawa, 1978; Slaw-  
 94 son & Savage, 1979). However, no surface ruptures were found by researchers in the days  
 95 and weeks following the rupture, and it remains unknown whether the BRF hosted the  
 96 1946 earthquake, or whether this fault is Quaternary-active or seismogenic.

97 In this paper, we undertake a field-based tectonogeomorphic investigation to eval-  
98 uate the seismogenic potential of the BRF and to determine its slip history and kine-  
99 matics with respect to historical seismicity and regional tectonics. We exploit a well-preserved  
100 set of offset paleochannels on the southwestern flank of the Beaufort Range, visible in  
101 recently acquired bare-earth lidar Digital Elevation Models (DEMs), to demonstrate that  
102 the BRF is a highly active, right-lateral transtensional fault that has hosted multiple surface-  
103 rupturing earthquakes throughout the Quaternary. We find evidence for at least three  
104 late Pleistocene to Holocene earthquakes along the BRF, with surface ruptures extend-  
105 ing  $>40$  km, consistent with paleo-earthquake magnitudes of  $\sim 6.5$  to  $7.5$ . While these  
106 data do not constrain the age of the most recent surface-rupturing event, our results do  
107 suggest that the most recent event occurred in the past  $\sim 3$ - $4$  kyr. We find that paleo-  
108 seismic earthquakes along the BRF have kinematics similar to the 1946 Vancouver Is-  
109 land earthquake, suggesting that the BRF is a candidate host fault for this event. Fi-  
110 nally, the similarities of the BRF deformation field and P- and T-axes derived from its  
111 slip over decadal to millennial timescales, suggest the stresses that lead to permanent  
112 deformation in this portion of the northern Cascadia forearc have been relatively con-  
113 sistent over multiple earthquake cycles.

## 114 **2 Background**

### 115 **2.1 Tectonic Setting**

116 The BRF is located in the northern forearc of the Cascadia subduction zone, where  
117 the Juan de Fuca plate subducts under the North American plate at a rate of  $\sim 43$  mm/yr  
118 (DeMets et al., 2010; Kreemer et al., 2014). The fault is positioned  $\sim 150$  km north of  
119 the Olympic Mountains, and  $\sim 60$  km south of the onshore projection of the Nootka fault  
120 zone, the northern end of the Juan de Fuca slab (Figure 1). Active faults that accom-  
121 modate forearc strain have been recognized along most of the Cascadia subduction zone  
122 south of the Olympic Mountains (e.g., Figure 1; Brocher et al., 2001; Goldfinger et al.,  
123 1992; Liberty et al., 2003; Personius et al., 2003; Sherrod et al., 2004; Kelsey et al., 2008;  
124 R. E. Wells et al., 2020; Horst et al., 2021), and north of the Olympic Mountains (e.g.,  
125 Figure 1; Schermer et al., 2021; Morell et al., 2017, 2018; Harrichhausen et al., 2021).  
126 However, no active faults have been identified in the northern 150-300 km of the fore-  
127 arc on Vancouver Island. It remains unclear if and how the slip accommodated by these

128 southern faults is translated farther north and what role the BRF may play in accom-  
129 modating forearc strain.

130 The BRF occurs along the southwestern flank of the Beaufort Range, near the city  
131 of Port Alberni on Vancouver Island (Figure 2a). The Beaufort Range consists of a  $\sim$ 70  
132 km long,  $\sim$ 5-10 km wide set of peaks, whose elevations range from 1000 to 1600 masl.  
133 The range is asymmetric, with a gently sloping, glacially scoured northeastern flank that  
134 slopes toward the Strait of Georgia, and a steep (up to  $35^\circ$ ) southwestern flank that slopes  
135 toward the Alberni Valley (Figure 2b). The BRF strikes NW-SE, following the south-  
136 western topographic range front for  $>40$  km (Figure 2b).

## 137 **2.2 Eocene slip along the Beaufort Range thrust fault**

138 The BRF has been previously mapped as an Eocene bedrock fault that places the  
139 Late Triassic Karmutsen Formation basalts that form the peaks of the Beaufort Range  
140 over the Cretaceous Nanaimo Group sediments that underlie the Alberni Valley (Figure  
141 2a, Figure S1; Yorath, Clowes, et al., 1985; T. England & Calon, 1991). Geologic map-  
142 ping, balanced cross sections, and LITHOPROBE seismic reflection profiles suggest this  
143 bedrock thrust fault dips NE, at  $45^\circ$  to sub-vertical (Yorath, Clowes, et al., 1985; Yorath,  
144 Green, et al., 1985; Clowes et al., 1987). Geologic maps depict the BRF as an along-strike  
145 projection of the frontal thrust fault of the Cowichan Fold and Thrust System (CFTS),  
146 located  $\sim$ 40 km along strike to the southeast of the BRF (Cui et al., 2017; T. England  
147 & Calon, 1991). Low-temperature thermochronology data indicating exhumation at  $\sim$ 50-  
148 40 Ma suggest the thrust faults of the CFTS, including the BRF, initially formed dur-  
149 ing the Eocene accretion of the Pacific Rim and Crescent terranes (T. D. J. England,  
150 1990; T. England & Calon, 1991; T. D. J. England et al., 1997).

## 151 **2.3 Glacial history**

152 The Beaufort Range and Alberni Valley experienced two major phases of glacia-  
153 tion during the last glacial period. The region was inundated by the south-southwestward  
154 flowing Cordilleran continental ice sheet during the Fraser stage glaciation ( $\sim$ 25-12 ka;  
155 Fyles, 1963; Alley & Chatwin, 1979). Then, during the retreat of the ice sheet, the Al-  
156 berni Valley was occupied by a southeastward flowing valley glacier that produced stream-  
157 lined landforms and associated glacial deposits (Mosher & Hewitt, 2004; Easterbrook,  
158 1992; Clague & James, 2002). Existing maps document sub-glacial till, colluvial, and al-

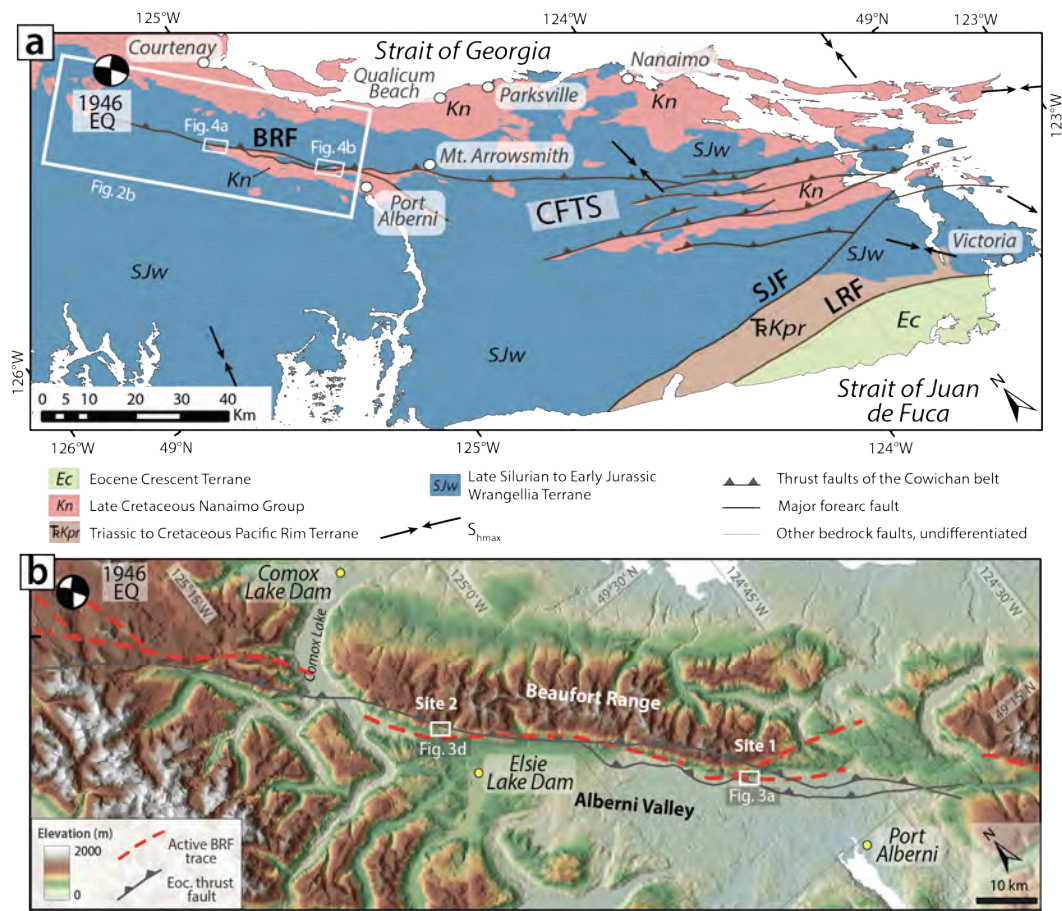


**Figure 2.** Geologic and geomorphic setting. **A:** Simplified geologic map of southern Vancouver Island showing major lithologic units, thrust faults of the Cowichan fold and thrust system (CFTS), and other forearc faults. The epicenter of the 1946 M 7.3 Vancouver Island earthquake is shown by the focal mechanism (Rogers & Hasegawa, 1978). Maximum horizontal stress directions after Balfour et al. (2011). Bedrock geology after the British Columbia Geological Survey compilation by Cui et al. (2017). BRF—Beaufort Range fault. LRF—Leech River fault. SJF—San Juan fault. **B:** Hillshaded SRTM DEM showing the topography of the Beaufort Range and Alberni Valley, the locations of hydroelectric dams, the trace of the Eocene bedrock Beaufort Range thrust fault (in legend), and a simplified inferred trace of the active BRF (in legend) based on the locations of mapped scarps (Supplemental Figure S1).

159    luvial deposits that extend to an elevation of  $\sim 300$  m along the range front (Fyles, 1963).  
160    These deposits have been correlated to the last glacial maximum at  $\sim 13.6$ -11 ka, based  
161    on ages from marine shells, peat, and wood in glaciomarine deposits in the Strait of Juan  
162    de Fuca and along the eastern coast of Vancouver Island (e.g., Clague, 1980; Easterbrook,  
163    1992). However, there has been limited surficial mapping of the Beaufort Range front,  
164    and no deposits in the Alberni Valley region have been directly dated. We expand and  
165    refine these mapping data to constrain the ages of deposits offset by scarps and evalu-  
166    ate the Quaternary activity of the BRF.

#### 167           **2.4 Possible association of the BRF with the 1946 Vancouver Island earth-** 168           **quake**

169           Although post-Eocene deformation has not been previously documented along the  
170           BRF, several researchers proposed that the Beaufort Range fault may have hosted the  
171           1946 M 7.3 Vancouver Island earthquake. The earthquake epicenter was located at the  
172           northern tip of the BRF at a depth of  $<30$  km, and focal mechanism solutions contain  
173           a NW-SE striking nodal plane sub-parallel to the BRF (Figure 2; Rogers & Hasegawa,  
174           1978). These data led Rogers and Hasegawa (1978) to propose that the 1946 earthquake  
175           may have been a right-lateral oblique event hosted by the BRF (Figure 2). Geodetic sur-  
176           veys of a triangulation network before and after the event suggest  $\sim 1$ -2.5 m of right-lateral  
177           oblique slip along a steeply NE dipping ( $70^\circ$ ) fault. While multiple ground surface fail-  
178           ures and slumps have been identified around the Beaufort Range associated with the 1946  
179           event (Mathews, 1979; Clague, 1996), no fault-related surface ruptures associated with  
180           the 1946 event were ever discovered.

### 181           **3 Methods**

182           Our methodological approach is motivated by newly available lidar bare-earth el-  
183           elevation models along the surface trace of the Beaufort Range fault that reveal a series  
184           of topographic scarps that suggest the fault has accommodated Quaternary offset (Fig-  
185           ure 2b). These scarps, clearly visible in bare-earth lidar DEMS (Figure 3), occur in en  
186           echelon arrays of 1-6 sets, each  $\sim 100$ -500 m long, and spaced 10s to 100s of meters apart.  
187           The majority of well-preserved scarps are located near the base of the range—20-100 m  
188           above the valley floor, or 500-870 m below the range crest—and strike sub-parallel to the  
189           trend of the southwestern flank of the Beaufort Range front ( $\sim 290$ - $320^\circ$ ; Figure 2b, Fig-

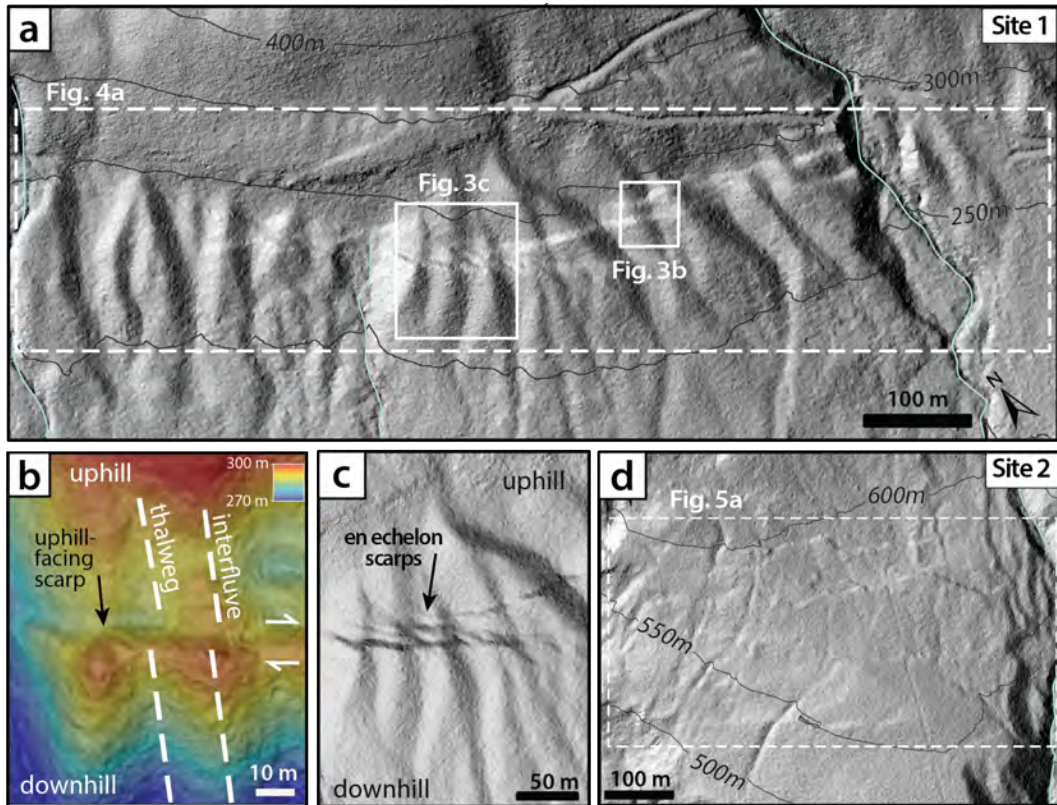


**Figure 3.** Examples of tectonic fault scarps visible in hillshaded bare-earth lidar DEMs.

**A:** Unannotated DEM of Site 1 showing a network of en echelon fault scarps offsetting a series of abandoned channels and interfluvial crests. **B:** Example of an uphill-facing scarp developed on a till-mantled hillside. The scarp offsets a channel thalweg and adjacent interfluvial crests both vertically (downhill-side-up) and right-laterally. **C:** Example of an en echelon array of scarps at Site 1. **D:** Unannotated DEM of Site 2 showing a network of right-laterally sheared channels. Examples of non-tectonic landforms are presented in Supporting Information Figure S2.

190 ure S1). Our initial observations of the lidar data suggested these scarps exhibit appar-  
191 ent right-lateral and SW-side-up 1-10-m scale displacement of a network of V-shaped pa-  
192 leochannels with paired offset sharp-crested interfluves. Given the glacial history of the  
193 region, we surmised that these channels may be no older than the time of ice retreat, and  
194 therefore the offset channels may record Holocene fault displacement.

195 Based on these initial observations, we undertook detailed field-based mapping and  
196 topographic surveying of faults and offset landforms to determine the geometry of the  
197 fault networks potentially associated with these scarps, the relative ages of offset deposits,  
198 the magnitude of potential offset, and the associated kinematics of fault slip.

### 199 3.1 Mapping

200 We completed surficial and bedrock mapping in order to: 1) identify earthquake-  
201 generated fault scarps along the BRF, 2) determine the relative ages of Quaternary de-  
202 posits offset by surface ruptures, and 3) determine if active fault strands re-occupied in-  
203 herited bedrock faults or shear zones. Identifying fault-related deformation (e.g., fault  
204 scarps) in datable Quaternary sediments is essential for characterizing the slip history  
205 of active faults (e.g., Van Der Woerd et al., 2002; Zinke et al., 2017; Hatem et al., 2017;  
206 Regalla et al., 2022), but dense temperate rainforest limits exposures and accessibility  
207 of offset Quaternary deposits in the study area. Thick soils and dense vegetative cover  
208 limit bedrock exposures to road cuts, logging roads, quarries, and stream channels, and  
209 obscure many Quaternary landforms beneath the forest canopy. However, these fault-  
210 related landforms are well-resolved in the newly available lidar point clouds collected along  
211 the BRF.

212 We used bare-earth lidar data, satellite imagery, and historical air photos to map  
213 potentially earthquake-generated fault surface ruptures (scarps) within a  $\sim 100$  km-long  
214 swath area extending from Mt. Arrowsmith to the Forbidden Plateau (Figure S1). Li-  
215 dar point cloud data were collected by Terra Remote Sensing, and TimberWest and Is-  
216 land Timberlands logging companies provided ground returns. The lidar point clouds  
217 contained an average of  $\sim 1.2$ - $1.4$  ground returns per square meter. We gridded these data  
218 into a 0.5 m DEM and generated topographic derivatives such as hillshade, standard de-  
219 viation, and slope maps to aid in mapping. We additionally used satellite imagery (Google  
220 Earth Pro, 2017) and British Columbia provincial government historical air photos from

1947 and 1952 to evaluate any anthropogenic modification of key sites, including past roads, railroads, and logging trails.

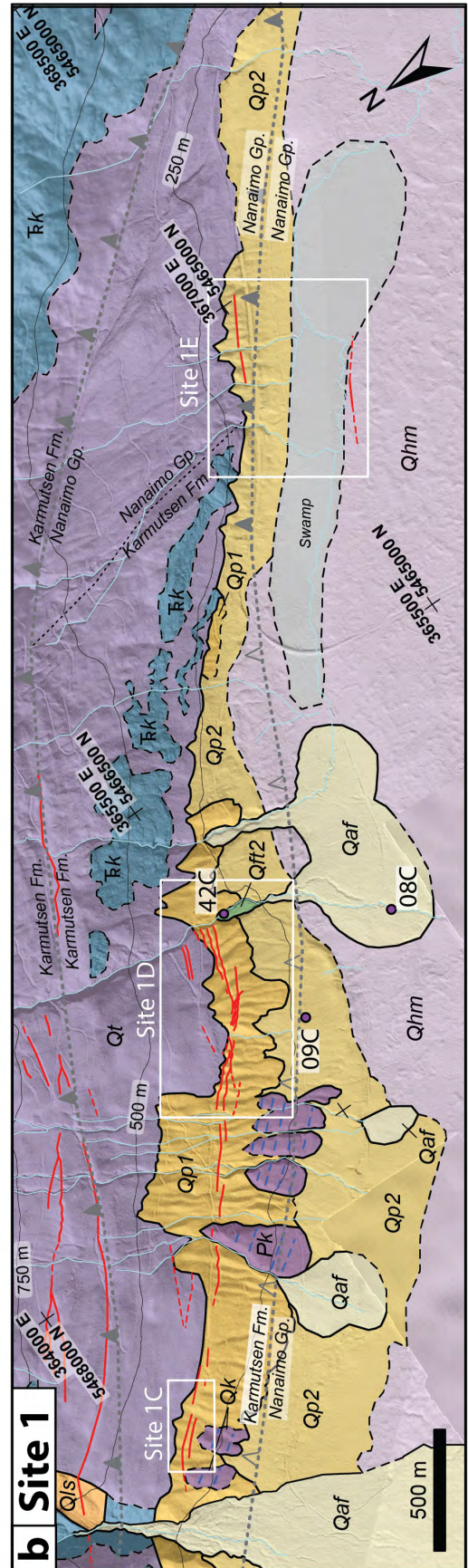
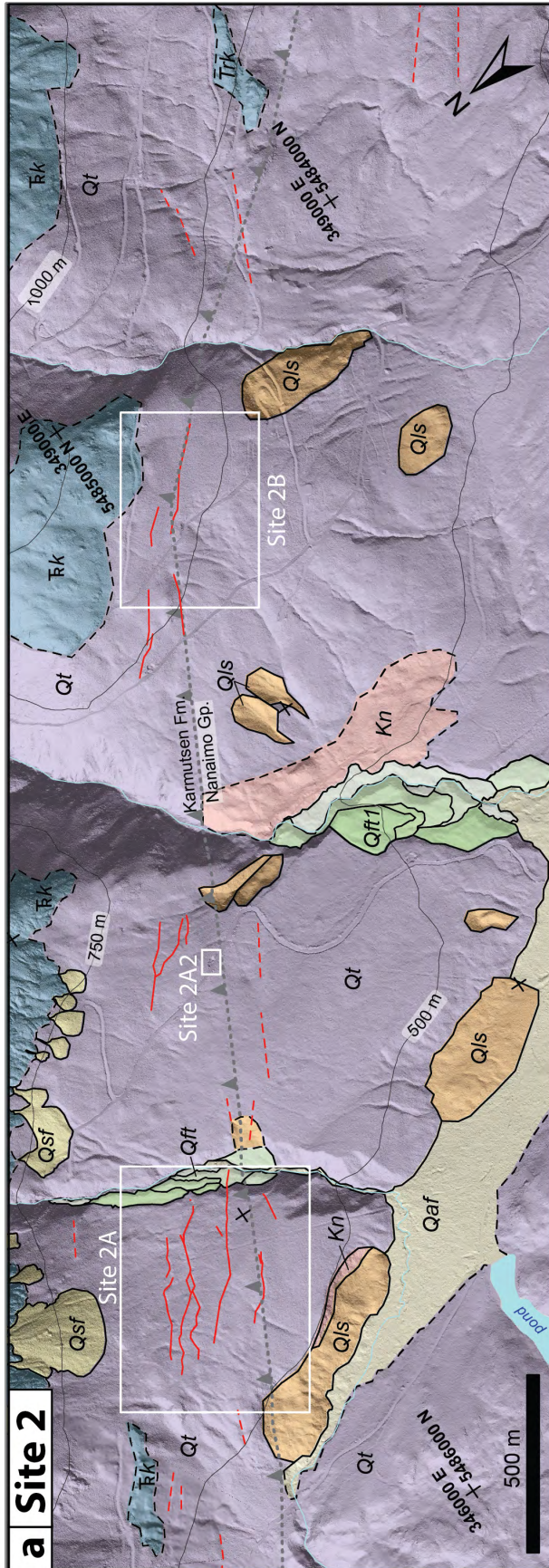
We visited each accessible remotely-mapped scarp to confirm they were tectonically-generated features (i.e., not related to slumping, etc.). Criteria used to distinguish fault scarps from other features include whether the features are linear, continuous over >50-100 m length scales, are cut across topography, and if they offset hillslopes, abandoned channels, or interfluves (Figure 3b-c). We took care to distinguish potentially fault-related scarps from landforms produced by glacial deposition or scour, anthropogenic disturbance, gravitational failure, or differential erosion (see Supporting Information Text S1 and Figure S2).

We then completed highly detailed and more focused field mapping, at a scale of 1:3000, of Quaternary deposits and bedrock units in two ~6 km by ~2 km regions (Sites 1 and 2) that each contain a high density of fault scarps (Figures 3, 4). Surficial mapping was completed based on field and lidar-based observations of surface topography, roughness, morphology, and inset and burial relationships, accompanied by detailed lithologic descriptions of each Quaternary unit. We used these observations to create a local Quaternary stratigraphy that allowed us to determine the relative ages of units offset by faults. Bedrock mapping was completed using outcrops exposed in road cuts, streams, and quarries. We measured the structural orientations of fault planes, slickenlines, foliation fabrics, and fractures within the principal shear zones and damage zones, where exposed.

## 3.2 Quantifying fault slip

### 3.2.1 Topographic surveys of offset landforms

We collected topographic survey data across fault scarps at 64 locations at Sites 1 and 2 in order to determine the attitudes of fault planes associated with fault scarps, and to quantify the vertical and lateral offset of displaced Quaternary deposits and landforms (Figures 5 and 6). These data included 58 surveys of offset geomorphic piercing lines where the three-dimensional oblique slip vector could be calculated (Figure 7), and 6 additional “straight-line” profiles used to calculate the vertical component of displacement in locations where geomorphic piercing lines were absent (Figures 5, 6, S4, and Dryad data repository Lynch et al., 2023). Surveys were collected with a Nikon XS and Spectra Precision Focus 6 total station, which yielded more continuous topographic data than



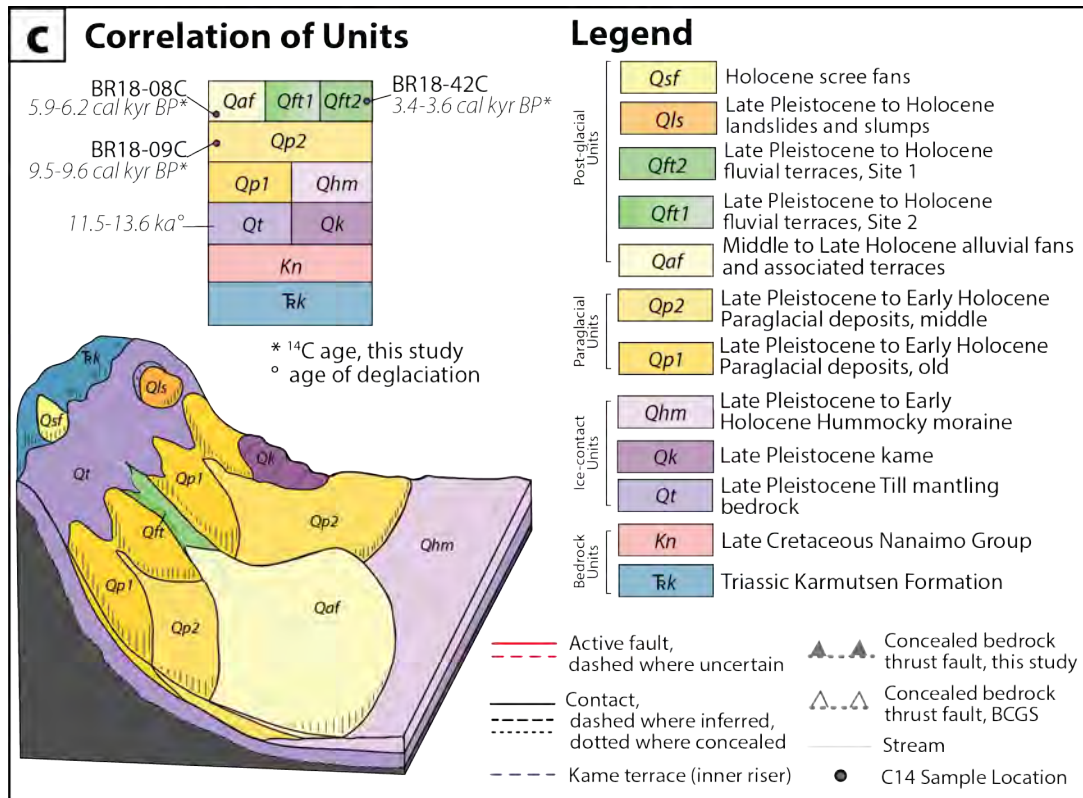


**Figure 4.** Bedrock and surficial geology of portions of the BRF (See locations in Figure 2a). Mapping is overlain on a composite hillshaded DEM compiled from two bare-earth lidar DEMs gridded to 0.5 m and to 2 m, and from 30 m SRTM DEM. Radiocarbon ages are reported in Table 1. Bedrock fault locations compiled from new field mapping and existing mapping by the British Columbia Geological Survey (BCGS; Cui et al., 2017). White boxes outlining Sites A-E correspond to locations shown in Figures 5 and 6. **A:** Map of Site 2 along the northern portion of the BRF. **B:** Map of Site 1, along the southern portion of the BRF. Fault scarps (red lines) occur at the base of the Beaufort Range and along the range front up to 1000 m above the valley floor. Mapped scarps occur in both the hanging wall and footwall of the bedrock BRF. Fault scarps offset multiple ages of glacial (Qt), paraglacial (Qp1, Qp2), and modern deposits (Qls, Qft, Qaf). Terrace generations within unit Qft1 in panel A are depicted by increasing color saturation with terrace age, delineated by thin gray lines. **C:** Correlation of units and legend for geologic maps in panels A and B. Radiocarbon ages demonstrate that these deposits are ~9600-3400 cal BP in age (Table 1).

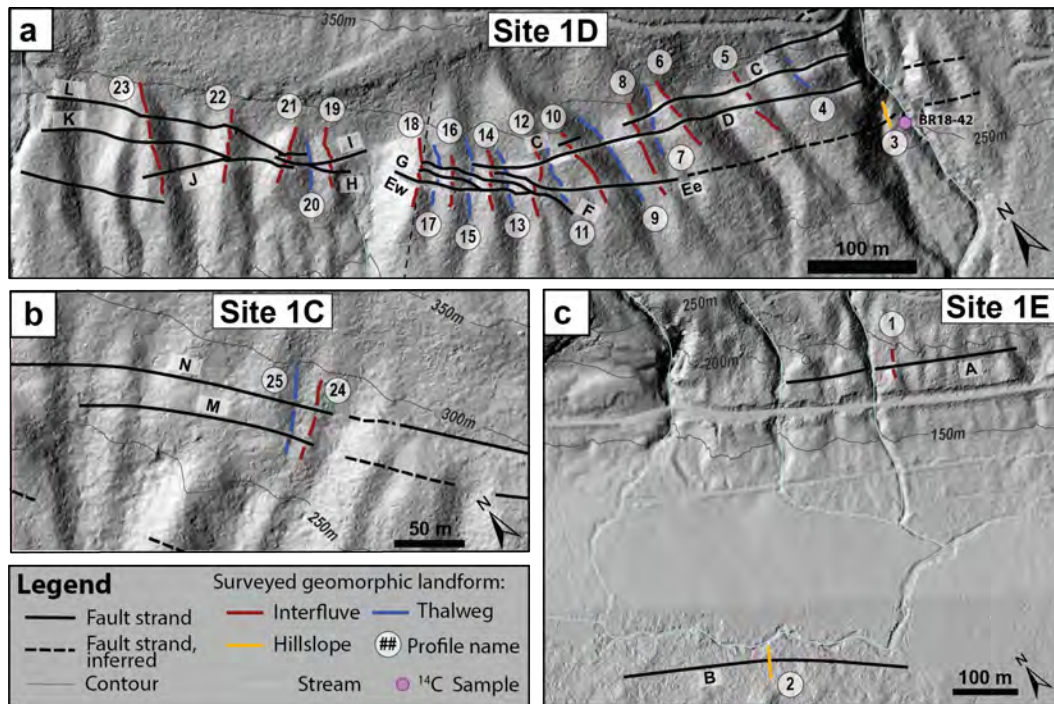


**Figure 5.** Hillshaded lidar DEMs of Site 1 showing mapped faults (labelled from A to N) and surveyed topographic profiles (numbered from 1 to 25). See Figure 4 for locations and Dryad data repository for topographic profile survey data (Lynch et al., 2023). **A:** Annotated hillshaded DEM showing the locations of mapped fault strands and topographic survey profiles at Site 1D. Unannotated lidar DEM is presented in Figure 3a. **B** and **C:** Annotated DEMs of Sites 1C and 1E. Unannotated versions of all DEMs are in Supporting Information Figure S3.

253 the lidar DEMs which had non-uniform return spacing and included some false ground  
 254 returns.

255 Our primary survey targets were a series of abandoned channels and interfluvial at  
 256 Sites 1 and 2 whose axes intersect fault scarps at near-orthogonal angles, that serve as  
 257 piercing lines from which fault slip vectors can be reconstructed. Topographic surveys  
 258 of these landforms followed either the channel thalweg or the interfluvial crest. In loca-  
 259 tions where channels and interfluvial are absent, we collected linear profiles with trends  
 260 perpendicular to the fault scarp. For each profile, total station survey data were collected  
 261 every  $\sim 0.5$ -1 m, to a distance of  $>20$  m uphill and downhill of each fault scarp (Figure  
 262 7). Along survey transects where a geomorphic piercing line extended for less than 20  
 263 m (e.g., between closely-spaced fault strands), we collected a minimum of 3 survey points,  
 264 with an average of 11 points. We complemented these ground surface elevation profiles

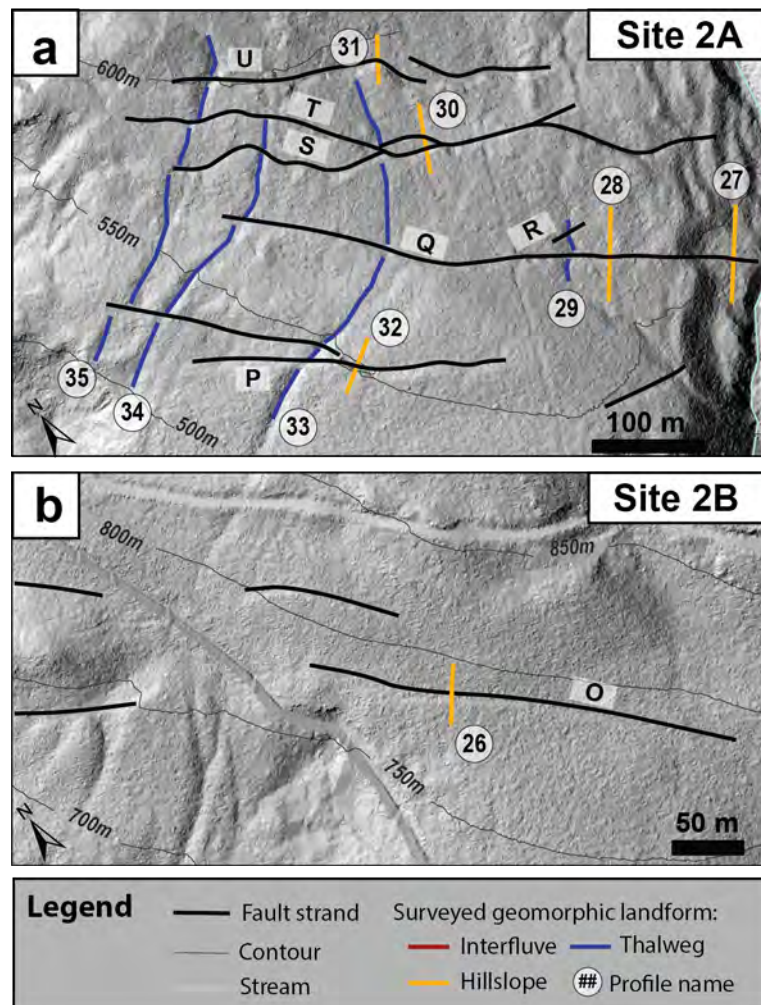


**Figure 6.** Hillshaded DEMs of Site 2 showing mapped faults (labelled from O to U) and surveyed topographic profiles (numbered from 26 to 35). See Figure 4 for locations and Dryad data repository for topographic profile survey data (Lynch et al., 2023). **A:** Annotated hillshaded DEM showing the locations of mapped fault strands and topographic survey profiles at Site 2A. Unannotated lidar DEM is presented in Figure 3d. **B:** Annotated DEM of Site 2B showing mapped faults and surveyed profile. Unannotated versions of all DEMs are in Supporting Information Figure S3.

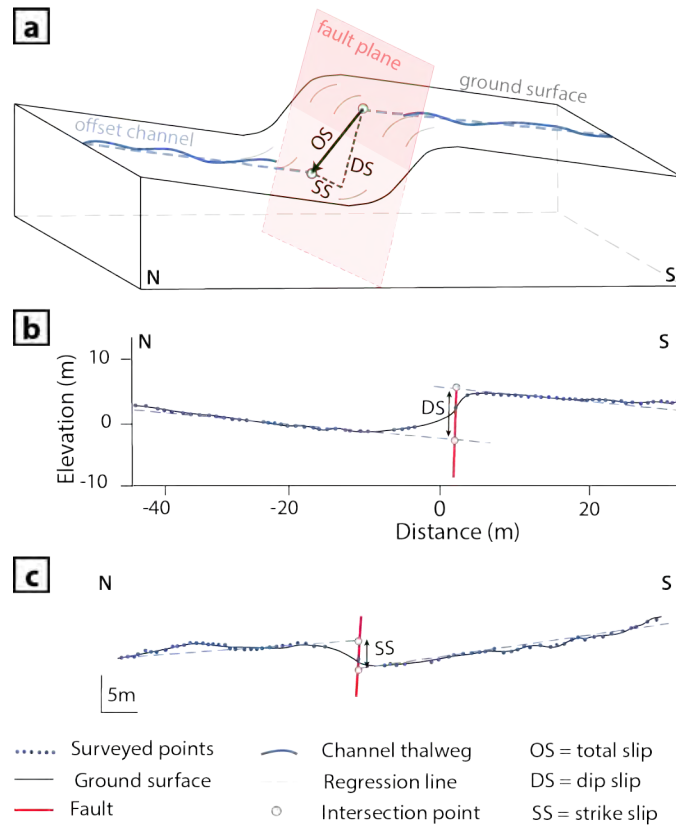


**Figure 7.** Schematic diagrams showing how surveyed geomorphic piercing lines were used to reconstruct 3D fault slip. **A:** Block diagram showing an oblique normal right lateral offset channel thalweg. Fault slip components (OS, DS, and SS) are calculated from the 3D positions of the intersections of the fault plane with the linear projections of the upthrown and downthrown channel segments. **B:** Example of a surveyed geomorphic piercing line profile in cross-section. **C:** Example of a surveyed geomorphic piercing line profile in plan view. In each survey, points were collected every  $\sim 0.5$ -1 m at least 10-20 m beyond the fault scarp.

265 with six additional topographic profiles extracted from lidar DEMs in a portion of Site  
 266 2A where thick forest cover and uneven topography prevented total station surveys of  
 267 offset abandoned channels.

### 268 **3.2.2 Reconstructing oblique fault displacement**

269 We used the topographic survey data to reconstruct both the magnitude and ori-  
 270 entation of the slip vector at each surveyed location where a geomorphic piercing line  
 271 intersected an individual fault plane. In order to calculate a slip vector, the local orien-

272 tation of the fault plane must be known. No outcrop exposures of fault planes in Qua-  
273 ternary deposits were present in the field area, but we were instead able to reconstruct  
274 the local strike and dip of the fault plane associated with mapped scarps using a mod-  
275 ified three-point problem approach. In this approach, we assumed the midpoint, or in-  
276 flection point, of a fault scarp represents the most likely intersection of the fault plane  
277 with the surface. We surveyed scarp midpoints at a range of elevations ( $\sim$ 4-12 m ele-  
278 vation range) and determined fault strike and dip through linear regression of a plane  
279 through the surveyed scarp midpoints using all surveyed data along a single continuous  
280 fault strand segment (3-17 points per regression). We used these data to determine a rep-  
281 resentative fault dip for each scarp segment, using the average dip from all regressions  
282 at Site 1 or Site 2, and a representative fault strike given by the local strike of each fault  
283 strand or segment. Because fault dips determined from surveys of degraded scarp faces  
284 over small elevation ranges may underestimate true fault dip, we allowed our model re-  
285 constructions to permit fault dip to be  $5^\circ$  steeper than that calculated from the three-  
286 point approach.

287 We combined our fault plane solutions and topographic survey data to calculate  
288 the 3D offset of each piercing line, specifically the magnitude and direction (trend and  
289 plunge) of the slip vector (Figure 7). Calculations were made using an R script that per-  
290 formed a Monte Carlo simulation to evaluate the slip vector and associated uncertainty  
291 (script available in data repository, Lynch et al., 2023). The script requires the follow-  
292 ing user-defined inputs: the strike and dip of the fault plane, the  $1\sigma$  uncertainty on strike  
293 and dip, the XYZ coordinates of the topographic survey data, the location where the fault  
294 plane intersects the ground surface, and the number of survey points in the upthrown  
295 and downthrown sides of the profile used to define the 3D geometry of the piercing line  
296 segments. For each profile, we assigned a fault strike and dip as described above, and  
297  $\pm 1\sigma$  uncertainty ( $5^\circ$ ). We manually defined the remaining parameters—fault plane in-  
298 tersections, and the number of survey points used to fit linear regressions through the  
299 upthrown and downthrown surveyed piercing lines—for each topographic profile. It has  
300 been well-documented that how a user defines fault and piercing line geometry (i.e., pro-  
301 file regression limits) can lead to multiple admissible geologic slip reconstructions (e.g.,  
302 Scharer et al., 2014). To account for this uncertainty, we performed Monte Carlo sim-  
303 ulations for each offset profile using input defined by five different users, each trained in  
304 scarp offset analysis.

305 Using these inputs, we used the R script to calculate 3D linear regressions through  
306 topographic survey points on the upthrown and downthrown sides of the fault scarp and  
307 then solve for the intersection points of these lines with the fault plane (Figure 7). These  
308 two intersection points were then used to calculate the magnitudes of strike slip (SS),  
309 dip slip (DS), and oblique slip (OS) for each piercing line, as well as the trend and plunge  
310 of the slip vector (Figure 7). The Monte Carlo simulation was repeated 100 times for each  
311 of the five user-defined profile selections, yielding a total of 500 simulations of fault slip  
312 for each displaced piercing line. We report the outputs as the mean  $\pm$  one standard de-  
313 viation of the 500 values calculated for that profile.

### 314 *3.2.3 Inversion for fault kinematics*

315 We use the slip vector data to invert for the kinematics of the BRF using the Fault-  
316 Kin 7.6 program (Marrett & Allmendinger, 1990; Allmendinger et al., 2012). Data in-  
317 puts included the trend and plunge of the best-fit slip vector determined from the Monte  
318 Carlo simulations, and the corresponding fault plane strike and dip determined from the  
319 modified three-point fault plane regressions. Inversions were performed using data from  
320 each of the 55 fault scarp surveys with vertically and laterally offset piercing lines. We  
321 grouped data for kinematic inversions in two ways. First, we grouped data collected at  
322 each mapping sub-site (A-E in Figure 4), to produce kinematic inversions representa-  
323 tive of slip observed at each site location. Then, we grouped all data for the entire BRF  
324 to determine a kinematic inversion best fit to all observed data. Kinematic inversions  
325 were performed by calculating P- and T-axes from each calculated slip vector and fault  
326 plane pair, and then generating Bingham fault plane solutions from the set of P- and T-  
327 axes at each site (Marrett & Allmendinger, 1990; Allmendinger et al., 2012). These in-  
328 versions assume slip occurs in the direction of maximum resolved shear stress on the fault  
329 plane, and produces mean P- and T-axes, pseudo focal mechanisms, and predicted slip  
330 vectors for each nodal plane (Marrett & Allmendinger, 1990; Allmendinger et al., 2012).  
331 These kinematic inversions and P- and T-axes provide information about paleo strain  
332 fields, and may, under certain assumptions, be used to approximate local stress axis ori-  
333 entations at the time of deformation (e.g., Angelier & Mechler, 1977; Riller et al., 2017).

### 3.3 Radiocarbon dating of Quaternary deposits

We collected charcoal samples from natural and manmade exposures of mapped Quaternary deposits to determine the chronologic ages of units offset by mapped faults. We focused our sampling on detrital charcoal as charcoal is present in many deposits on Vancouver Island, has previously been used to evaluate late Pleistocene to Holocene unit ages (e.g., Clague, 1980; Morell et al., 2018; Harrichhausen et al., 2021), and because luminescence techniques have not yielded reliable ages for late Pleistocene to Holocene deposits due to insufficient dose rate (e.g., Graham, 2017; Morell et al., 2018). We collected samples of macroscopic (macro) charcoal (>0.5 cm) where fragments were visible in outcrops of Quaternary deposits. If no macro charcoal was readily visible in an outcrop, we collected 1-2 L of bulk sediment and sieved the samples to extract any datable macro charcoal present. For all sample sites, we completed detailed unit descriptions and noted the sample's stratigraphic position within the deposit (Figure S3). We collected three macro charcoal samples and five bulk sediment samples from Site 1 (see Figure 4b for locations). Our sampling was focused on units mapped at Site 1 (Figure 4b), where we identified multiple generations of Quaternary deposits (see Section 4.2). We were unable to date any mapped deposits at Site 2 due to a lack of exposure.

Charcoal samples were cleaned and processed at Paleotec Services, Ottawa, Ontario, Canada. Macroscopic charcoal pieces were extracted from bulk sediment samples by flotation and wet sieving in warm tap water using nested sieves of 0.85 mm and 0.425 mm. All material greater than 0.425 mm was examined using a binocular microscope, and any isolated charcoal pieces were shaved of any adhering sediment. The largest shaved fragment from each sample was further sliced into smaller fragments to look for the presence of fine modern rootlet penetration and/or fungal contamination, including mycorrhizae, and rejected if contaminants were present.

Three Quaternary units yielded datable charcoal fragments that were processed for radiocarbon analysis (Table 1, Figure 4b). These included macro charcoal samples extracted from one outcrop (BR18-06C, -07C, and -08C), and two samples extracted from sieved bulk sediment from two additional outcrops (BR18-42C and BR18-09C). Sample BR18-08C was selected as the highest quality sample of the three charcoal fragments extracted from the outcrop exposure. Bulk sediment sample BR18-09C included three mm-sized charcoal pieces that were combined to ensure adequate sample mass for AMS after acid-base-acid (ABA) treatment (Table 1, Figure 4b, Figure S3). Unfortunately, the

367 three remaining bulk sediment samples (BR18-10C, -11C, and -12C) were barren of char-  
368 coal. Samples were analyzed at the Keck Carbon Cycle AMS Laboratory at UC Irvine.  
369 Radiocarbon ages (reported following Stuiver & Polach, 1977) were calibrated using the  
370 INTCAL20 calibration curve (Reimer et al., 2020) and OxCal v4.4 (Bronk Ramsey, 1995,  
371 2021). We report radiocarbon ages as the two-sigma ( $2\sigma$ ) range of calendar years before  
372 present (1950).

### 373 **3.4 Estimates of fault slip**

374 We estimate slip rates at Site 1 using the cumulative oblique displacement mea-  
375 surements of three different ages of offset landforms, as well as radiocarbon dates from  
376 detrital charcoal that provide estimates of unit ages. We use two approaches to estimate  
377 slip rates, following the methods of DuRoss et al. (2020). The first is an “open-ended”  
378 approach that uses the cumulative slip of the oldest offset unit and that unit’s estimated  
379 age. The second is a “closed interval” approach that uses the difference in slip that has  
380 occurred during a known time interval that encompasses one or more complete recur-  
381 rence periods. We report both slip rate calculations and discuss the relative applicabil-  
382 ity of each.

## 383 **4 Results**

384 Our mapping provides several lines of evidence that the BRF is Quaternary-active,  
385 and has experienced multiple slip events since the late Pleistocene. Field mapping of the  
386 morphology and spatial distribution of fault scarps (Figures 3 and 4) indicates that the  
387 mapped scarps are of tectonic origin, produced during one or more surface-rupturing earth-  
388 quakes, and are not the product of glacial, gravitational, or anthropogenic processes. An  
389 active BRF is further supported by the presence of numerous right-laterally and verti-  
390 cally offset abandoned stream channels incised into Late Pleistocene to Holocene till and  
391 paraglacial deposits. Below we discuss the morphology of the fault scarps, the ages of  
392 offset deposits, the kinematics of fault slip derived from measured offsets of channel net-  
393 works, and our interpretations of the number and relative timing of events that have oc-  
394 curred along the BRF since the last glacial maximum.

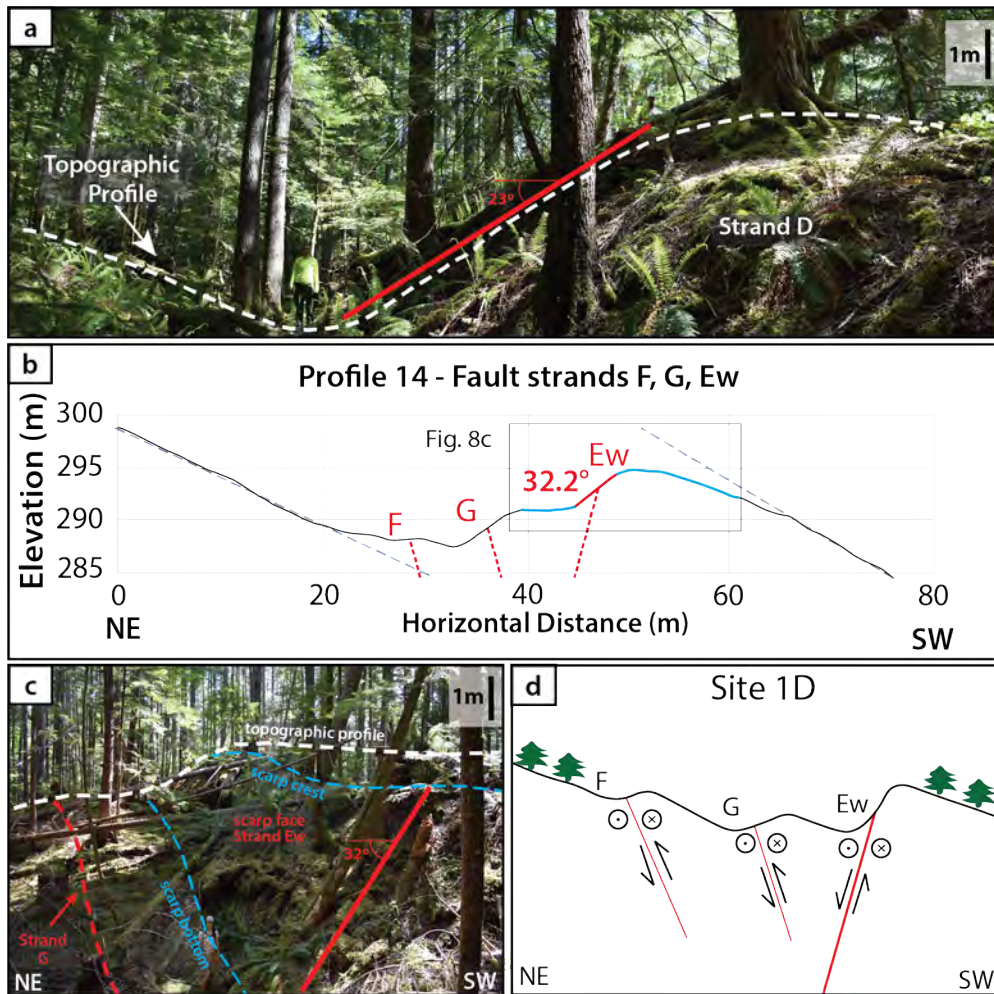


**Figure 8.** Examples of fault scarps identified along the Beaufort Range fault. **A:** Tall, uphill-facing, moderately steep ( $\sim 23^\circ$ ) fault scarp along strand D at Site 1D (Figures 4b, 5a). **B:** Topographic profile across three scarps at Site 1D associated with fault strands F, G, and Ew extracted from bare-earth lidar DEM (Profile 14, Figure 5). Dashed dark blue lines show the projection of the background hillslope toward the scarps. **C:** Photo of the tall, steep preserved face of Strand Ew shown in the topographic profile in panel b. The uphill-facing fault scarp along strand Ew is  $\sim 32^\circ$ , nearly angle of repose, much steeper than the scarp face along strand D (panel a). **D:** Cartoon cross-section showing the schematic relationships between sets of sub-parallel and en echelon fault strands, based on observations at Site 1D. These strands are interpreted to merge at depth in a flower structure consistent with strike-slip faulting.

#### 4.1 Quaternary fault scarps

Our mapping shows that the Quaternary-active BRF is defined by a series of sub-parallel, discontinuous fault scarps (n=153) that offset multiple ages of Quaternary deposits preserved on the southwestern flank of the Beaufort Range (Figure 2a, Figure S1). The spatial distribution of preserved scarps shows they are part of an ~500 m wide fault zone, where slip is distributed across multiple (~1-6) sub-parallel, steeply-dipping fault strands (Figure 8, Figure S1). Individual fault scarps locally exhibit strike lengths of ~100-1500 m, exhibit scarp heights of ~0.5-6 m, and occur in en echelon or parallel sets with intra-fault spacings of 5-100 m. Scarp facing directions can vary locally over short distances but about two thirds of the scarps (n=101) face NE. Most (~70%) of the mapped faults have asymmetric cross-sectional morphologies with steep uphill-facing scarps, while a smaller fraction are preserved as flat, degraded topographic features embedded in the high-gradient hillslopes (Sites A-E; Figures 3, S2, S4). Our mapping demonstrates that active fault strands generally strike NW, parallel to the range (average ~287°, with variation of up to 20°-38°), and our topographic field surveys (see Section 3.2.2) indicate that near the surface, most strands dip steeply NE (~60°-88°), with a few dipping steeply SW (~70°).

The steepness and morphology of the scarp faces vary both along strike and between strands. At Site 1, the steepest and tallest scarps are 4-6 m tall and have scarp faces near the angle of repose (32° strand Ew at Site 1D; Figures 5, 8). Many of the scarps at Site 1 exhibit steep, well-preserved free faces, such as strand Ew at Site 1D (Figure 8b-c). Other scarps at Site 1 exhibit a more moderate, 24° dipping scarp face (Figure 8a), such as Strand D at Site 1D. At Site 2, the scarps are 1-3 m tall and have faces near the angle of repose (~45° strand U at Site 2A; Figures 6 and S5), and some are large and steep enough to have effectively ponded large boulders sourced from uphill (Figure S5). Several of the individual scarps at Site 1 are part of a larger, multi-fault scarp that includes multiple emergent fault strands (Figure 8b), whereas individual scarps at Site 2 appear to occur as separate parallel or anastomosing fault sets (Figure 6).

Our mapping shows that the majority of active fault scarps are not directly co-located with known bedrock fault planes at the surface (Figures 4 and S1). At Site 2, the primary bedrock thrust fault, which places Karmutsen Fm basalts over Nanaimo Gp sediments (Figure 4a), is exposed as a 200+ m wide damage zone that juxtaposes hanging wall basalts against an upright, open, footwall syncline of Nanaimo Gp sandstones. Mapped

428 Quaternary fault scarps do not appear co-located with the exposed bedrock fault plane  
 429 at the surface, but instead occur in sub-parallel networks spanning up to 500 m away,  
 430 in both the hanging wall and footwall. Similarly, at Site 1 where the bedrock thrust branches  
 431 into two strands, mapped Quaternary faults occupy a zone that is  $\sim 500$  m wide, and oc-  
 432 cur up to 500 m away from mapped bedrock thrust faults (Figure 4b).

433 Quaternary fault scarps also have different slip senses and attitudes than observed  
 434 along the bedrock thrust faults. Slickenlines and Riedel shear geometries (Figure S7) on  
 435 Eocene bedrock thrust faults indicate apparent NE-side-up, dominantly dip-slip displace-  
 436 ment, whereas the active faults exhibit southwest-side-up and right-lateral displacements  
 437 (Figure S7). Outcrop exposures of the bedrock thrust fault at both Site1 and Site 2 ex-  
 438 hibit strike orientations that differ from Quaternary scarps by  $\sim 15^\circ$ . Our field surveys  
 439 indicate that the active fault BRF strands have dips of  $70^\circ$ - $90^\circ$  NE, whereas exposures  
 440 at several sites along the range suggest the inherited thrust fault has a dip of  $<40^\circ$  NE  
 441 to sub-vertical. These observations indicate that mapped active fault scarps are not pro-  
 442 duced by slip along inherited structures in the near subsurface, but instead occupy a zone  
 443 that is generally sub-parallel to the inherited structure.

## 444 **4.2 Quaternary mapping and stratigraphy**

445 Quaternary fault scarps along the BRF displace a series of nine units that were de-  
 446 posited during the late Pleistocene to Holocene deglaciation and subsequent transition  
 447 to a post-glacial environment. We develop a local Quaternary stratigraphy (Figure 4 and  
 448 Table S1) that groups these deposits into three categories: ice-contact glacial units de-  
 449 posited during the most recent glaciation, paraglacial units deposited during ice retreat  
 450 and slope readjustment, and post-glacial units deposited after ice retreat.

### 451 ***4.2.1 Ice-contact glacial deposits and landforms***

452 The ice-contact glacial units are the oldest and stratigraphically lowest Quaternary  
 453 units mapped in the study area and include subglacial till (Qt), kame terraces (Qk), and  
 454 hummocky moraine (Qhm) (Figure 4; Table S1). The subglacial till (Qt) is a very in-  
 455 duredated, matrix-supported diamict containing both locally-derived and exotic clasts and  
 456 is up to 40 m thick. Qt mantles bedrock along the southwestern flanks of the Beaufort  
 457 Range mountain front at elevations  $>150$ - $400$  m. Kame terraces (Qk) occur as a series  
 458 of five evenly-spaced, flat-topped terrace treads with steep risers, at  $150$ - $300$  masl ( $<150$

459 m above the valley floor), underlain by indurated, poorly to moderately sorted, strat-  
 460 ified sands and gravels. Hummocky moraine (Qhm) is present on the valley floor at el-  
 461 evations of <150 masl at Site 1.

#### 462 ***4.2.2 Paraglacial deposits and landforms***

463 Glacial deposits are overlain by two generations of paraglacial deposits, Qp1 and  
 464 Qp2 (Figure 4c; Table S1). Qp1 consists of indurated, clast-supported, poorly-sorted,  
 465 stratified sands and gravels. Qp1 deposits occur as cone-shaped landforms whose heads  
 466 merge into Qt and whose toes are buried by Qp2 at the foot of the range. Qp2 has a sim-  
 467 ilar composition to Qp1 and consists of thinly-bedded, clast-supported, stratified sands  
 468 and gravels with occasional coarse sand lenses. Qp2 is distinguishable from Qp1 based  
 469 on inset and burial relationships and its position at lower elevations on the range front.

470 Qp1 is incised by a series of abandoned channels. These channels are disconnected  
 471 from active streams but merge into the heads of Qp2 deposits, suggesting that they were  
 472 active at the time of deposition of Qp2. Abandoned channels at Site 1 are typically ~1-  
 473 4 m deep, have V-shaped cross-sectional morphologies and are separated by adjacent in-  
 474 terfluves with linear ridges and steep flanks, or are incised into till and colluvium-mantled  
 475 hillslopes (Figures 3 and 4). We interpret these abandoned channels to have formed as  
 476 the result of fluvial and debris flow scouring and filling associated with the deposition  
 477 of Qp2. At Site 2, offset abandoned channels have broad cross-sectional morphologies  
 478 and are moderately incised into hummocky, till-mantled hillslopes (Figures 3 and 4). These  
 479 channels do not clearly merge into other mapped deposits but appear to be cross-cut by  
 480 younger landslides at the foot of the range.

#### 481 ***4.2.3 Post-glacial units and landforms***

482 The youngest units include post-glacial landslides (Qls), scree fans (Qsf), alluvial  
 483 fans (Qaf), and fluvial terraces (Qft1 and Qft2) that either bury or are inset into the glacial  
 484 and paraglacial deposits (Figure 4, Table S1). Mapped landslides (Qls) are hummocky  
 485 deposits associated with curvilinear headscarps and oversteepened toes and have widths  
 486 of 50-600 m. Scree fans (Qsf) are small (30-250 m across), fan-shaped deposits with rough  
 487 surfaces that contain cobble to boulder-sized bedrock clasts. Qsf occurs at the bases of  
 488 mapped bedrock exposures at elevations of ~750 masl. Alluvial fan deposits (Qaf) are  
 489 defined as a series of broad, convex, gently-sloping fans headed in active or recently-active

490 channels (Figure 4). The fans consist of poorly to moderately sorted, clast-supported,  
491 stratified alluvial and fluvial deposits containing silt, sand, pebbles, and boulders, with  
492 occasional clast imbrication and cross-bedding (Table S1). Qaf deposits are mapped at  
493 the base of the range front and bury portions of Qp2, Qt, and Qhm.

494 At two locations in Site 2, and one at Site 1, Qaf fan heads merge into deeply in-  
495 cised (by  $\sim 1\text{-}15$  m) streams that are flanked by a series of up to five fluvial terraces (Qft1  
496 and Qft2). Fluvial terrace treads are 20-130 m wide, slope gently downstream, and have  
497 risers up to 5-10 m tall. The deposits that underlie these terraces are moderately to well-  
498 sorted, clast-supported sediments, with sub-horizontally stratified interbeds of rounded  
499 cobbles, boulders, and pebbles. We subdivide these fluvial terraces into two generations  
500 (Qft1 and Qft2) based on the inset relationships observed at Sites 1 and 2. At Site 2,  
501 Qft1 terraces are inset into till-mantled bedrock and are, in turn, incised by channels feed-  
502 ing Qaf alluvial fans (Figure 4b). This observation shows that at Site 2, Qft1 terraces  
503 are older than Qaf. In contrast, at Site 1, Qft2 appears to grade into the channels that  
504 feed Qaf, indicating that Qft2 terraces are younger than at Site 1 and are instead cor-  
505 relative to upper portions of Qaf or the channels inset into Qaf (Figure 4a).

#### 506 *4.2.4 Radiocarbon results and inferred unit ages*

507 We use radiocarbon ages from detrital charcoal extracted from Quaternary deposits  
508 to place brackets on the possible ages of mapped units offset by BRF scarps. We note  
509 that the interpretation of detrital charcoal radiocarbon dates can be challenging due to  
510 vertical mixing during bioturbation or soil creep, recycling of older charcoal into younger  
511 deposits, and bias from younger carbon (e.g., roots) included in older charcoal. However,  
512 the radiocarbon ages that we obtained from Quaternary units in the map area are in broad  
513 agreement with our local relative Quaternary stratigraphy (Figure 4) and with regional  
514 constraints on the timing of deglaciation and post-glacial processes (e.g., Halsted, 1968;  
515 Alley & Chatwin, 1979; Blaise et al., 1990; Clague, 1994). We use these data, therefore,  
516 to make the following interpretations of unit ages.

517 The three ice-contact glacial deposits, Qt, Qk, and Qhm, were barren of charcoal  
518 and could not be directly dated (Table 1). This absence is consistent with other stud-  
519 ies on Vancouver Island that have found ice-contact deposits to be devoid of charcoal  
520 (Morell et al., 2018; Harrichhausen et al., 2021). We interpret Qt, Qk, and Qhm to be  
521 associated with the last glacial maximum, which has been regionally dated to  $\sim 11.5\text{-}13.6$

522 ka (Halsted, 1968; Alley & Chatwin, 1979; Blaise et al., 1990; Clague, 1994), although  
523 we recognize the possibility that deposits associated with prior glacial periods may be  
524 present in the study area.

525 We attempted to radiocarbon date both Qp1 and Qp2 debris-cone fan deposits, but  
526 only Qp2 yielded datable charcoal. The charcoal sample was collected from a stratified  
527 fan deposit  $\sim 30$  cm below the surface of Qp2 (BR18-09C), in a roadcut exposure located  
528  $\sim 250$  m SW of the fault scarps at Site 1 (Figure 4, Figure 3). This sample yielded an  
529 age of  $\sim 9.5$  cal ka (Table 1), consistent with the older estimated age of the Late Pleis-  
530 tocene glacial deposits (Qt, Qk, and Qhm) of  $\sim 11.5$ - $13.6$  ka, and younger radiocarbon  
531 ages of samples from Qaf and Qft2 (see below). The  $\sim 9.5$  cal ka age is also broadly con-  
532 sistent with the timescales of paraglacial debris cone formation documented in recently  
533 deglaciaded terrains that suggest these types of deposits form in the first 100s-1000s of  
534 years following deglaciation (Ryder, 1971; Ballantyne & Benn, 1996; Ballantyne, 2002).

535 Post-glacial units Qaf and Qft2 also yielded datable macro-charcoal fragments. Qaf  
536 yielded one macro-charcoal sample (BR18-08C). This sample was collected from a strat-  
537 ified, clast-supported sand lens within interbedded sands and gravels  $\sim 0.75$  m below the  
538 top of the deposit located  $\sim 500$  m SW of fault scarps at Site 1 (Figure 4 and 3). This  
539 sample yielded a radiocarbon age of  $\sim 6$  cal ka (Table 1). Qft2 yielded a charcoal sam-  
540 ple (BR18-42C) sieved from bulk sediment collected from a stream cut exposure of strat-  
541 ified pebbles and cobbles, located  $< 10$  m downhill from mapped fault strand Ee (Fig-  
542 ure 4b, Figure 3). This sample yielded a radiocarbon age of  $\sim 3.5$  cal ka (Table 1). Both  
543 ages are younger than the ages determined from a radiocarbon sample from paraglacial  
544 deposit Qp2 ( $\sim 9.5$  cal ka), and agree with our stratigraphic interpretation that Qaf is  
545 older than Qft2.

546 If we assume that these samples reflect deposit ages, and are not significantly al-  
547 tered by recycling, bioturbation, or inclusion of younger carbon, these data suggest the  
548 following as possible brackets on the ages of mapped deposits. Qt, Qk, and Qhm are likely  
549  $\sim 11$ - $14$  ka, paraglacial deposits Qp1 and Qp2 are likely  $\sim 6$  to  $\sim 11$  ka, Qaf units are likely  
550  $\sim 3$  to  $\sim 9$  ka, and Qft2 deposits are likely  $< 4$  ka. Given the uncertainties inherent with  
551 this method and with the small number of samples available for dating, we treat these  
552 as age approximations.

**Table 1.** Radiocarbon sample data at Site 1D (see Figures 4b and 4c for locations).

Unit <sup>a</sup>	Coordinates <sup>b</sup>	Sample Name	Sample Type	Dated Material	UCIAMS ID <sup>c</sup>	Fraction Modern	D14C (‰)	Radiocarbon Age <sup>d</sup> (years BP, 2 $\sigma$ )	Calibrated Age <sup>e</sup> (cal BP)
Qft2	364944 E, 5466432 N	BR18-42C	Bulk sediment	Charcoal (single piece)	215248	0.6658 $\pm$ 0.0013	-334.2 $\pm$ 1.3	3265 $\pm$ 20	3560-3400
	Qaf	BR18-06C	Macro charcoal	Not dated	-	-	-	-	-
BR18-07C		Macro charcoal	Not dated	-	-	-	-	-	
BR18-08C		Macro charcoal	Charcoal (single piece)	215248	0.5185 $\pm$ 0.0010	-481.5 $\pm$ 1.0	5275 $\pm$ 20	6180-5940	
Qp2	364400 E, 5466402 N	BR18-09C	Bulk sediment	Charcoal (composite of three pieces)	215249	0.3428 $\pm$ 0.0008	-657.2 $\pm$ 0.8	8600 $\pm$ 20	9600-9520
	0364683E, 5466207N	BR18-10C	Bulk sediment	barren	-	-	-	-	-
Qp1	0365209E, 5466352N	BR18-11C	Bulk sediment	barren	-	-	-	-	-
	0364515E, 5466653N	BR18-12C	Bulk Sediment	barren	-	-	-	-	-

<sup>a</sup> See Figure 4 and Table S1<sup>b</sup> NAD83 UTM Zone 10<sup>c</sup> Samples were prepared at PaleoTek Services. Sample preparation backgrounds have been subtracted, based on measurements of<sup>d</sup> <sup>14</sup>C-free wood. These samples were treated with acid-base-acid (1N HCl and 1N NaOH, 75 °C) prior to combustion. Samples were processed at the UC Irvine Keck AMS facility.<sup>e</sup> All results have been corrected for isotopic fractionation according to the conventions of Stuiver and Polach (1977), with <sup>d13</sup>C values measured on prepared graphite using the AMS spectrometer. These can differ from <sup>d13</sup>C of the original material, and are not shown.<sup>e</sup> Radiocarbon ages calibrated using INTCAL20 (Reimer et al., 2020) and OxCal v. 4.4 (Bronk Ramsey, 2021). Range reported represents unmodeled 95% confidence interval as calculated by OxCal.

### 4.3 Fault offset measurements

Results of our field mapping and topographic surveys show that the BRF has accommodated several meters of vertical and right-lateral displacement, distributed over a network of one to six fault strands that offset the mapped late Pleistocene to Holocene deposits (Figure 3). At Site 1 (Figure 5), scarp heights on individual fault strands range from 0.5 to 6 m, and channels appear in the field to be right-laterally offset by  $\sim 0.5$ -2 m. These observations suggest cumulative displacements of several meters across multiple fault strands. Similarly, at Site 2, scarp heights range from 1 to 3 m, and a series of three stream channels visible in lidar appear to be systematically right laterally sheared by several meters across three to five fault strands (Figure 6). Our field observations and survey data also show that scarp heights in older deposits and landforms, including the interfluves developed in Qp1 at Site 1 and the till-mantled hillslopes at Site 2, have larger vertical displacements than the younger channels incised into these deposits, suggesting the potential for multiple events.

#### 4.3.1 Slip vectors and fault kinematics

Estimates of slip based on our topographic survey data confirm our field observations that the BRF exhibits consistent right-lateral and dip-slip offset of the ground surface. Oblique slip magnitudes across individual fault strands range from  $\sim 2$  to 7 m at Site 1 and from  $\sim 2$  to 5 m at Site 2 (Table S2). Average dip-slip magnitudes for single faults range from  $\sim 1$  to 5 m, with the largest dip-slip magnitudes of up to  $\sim 9$  m observed at Site 1D (Table S2). Average right-lateral strike-slip magnitudes recorded in offset channels and interfluves at Sites 1 and 2 range from  $\sim 1$  to 5 m. Displacements of piercing lines across individual strands yield a  $\sim 0.3:1$  to  $1.5:1$  ratio of strike slip to dip slip, similar to those yielded by the cumulative displacements (Table S2). These data suggest that, while the fault system as a whole accommodates approximately equal magnitudes of strike slip and dip slip, some individual fault strands are dominated by dip slip, while others are dominated by strike slip.

Kinematic inversions of BRF slip vector data produce pseudo focal mechanisms that similarly indicate right-lateral transtension along a steeply NE-dipping fault (Table S3). Inversions performed for Sites 2A, 1C, 1D, and 1E (Figure 9 a-d) show small variations in the average strike and dip of the primary slip plane of  $292$ - $321^\circ$  and  $66$ - $78^\circ$ , and in the average trend ( $095$ - $153^\circ$ ) and plunge ( $10$ - $26^\circ$ ) of the model slip vectors. These site-specific

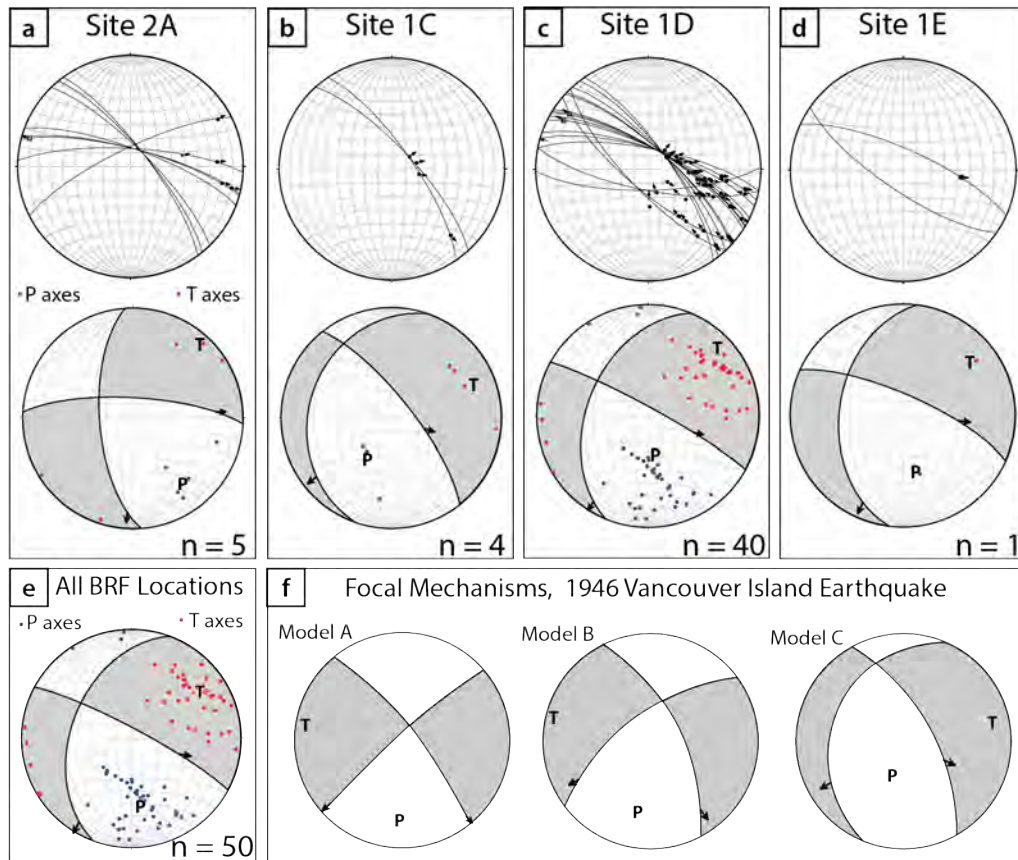


**Figure 9.** Right-lateral transtension along the Beaufort Range fault demonstrated by slip vectors and pseudo focal mechanisms produced from kinematic inversions. **A-D:** Kinematic data at four sub-sites along the BRF (see Figure 4 for locations). Upper panels: Lower hemisphere equal area projections showing fault planes, slip vectors, and hanging-wall motions. Lower panels: P- and T-axes and linked Bingham fault plane solutions (lower) for faults at locations 2A, 1C, 1D, and 1E. These slip vectors and kinematic inversions are consistent with right-lateral oblique motion on NE-dipping planes. **E:** Composite kinematic inversion for all surveyed sites along the BRF. Lower hemisphere equal area projection showing P- and T-axes and linked Bingham fault plane solutions. **F:** Focal mechanism solutions for the 1946 M 7.3 Vancouver Island earthquake (Rogers & Hasegawa, 1978, see Figure 2a for epicentrallocation). Model A is Rogers and Hasegawa’s preferred model. Note the similarity in orientations of nodal planes and P- and T-axes for BRF fault kinematics.

585 inversion data are similar to full fault inversions, and indicate an approximate slip trend  
 586 and plunge of  $\sim 110/45$  along an  $\sim 80^\circ$  NE dipping fault plane. These full-fault pseudo  
 587 focal mechanisms yield local P- and T-axes with trends and plunges of  $170/37$  and  $058/26$   
 588 respectively.

#### 589 **4.3.2 Cumulative displacements**

590 At Site 1, available exposures allowed us to calculate cumulative displacement across  
 591 one to three strands for 14 interfluves developed in Qp1 and 9 channels incised into Qp1  
 592 (Figure 5). These data show that cumulative oblique slip at Site 1 measured in offset  
 593 interfluves and channels ranges from  $\sim 4$  to 21 m (Figure 6). At Site 2, cumulative dis-  
 594 placement of channels incised into Qt was summed across two to four mapped strands  
 595 showing cumulative slip magnitudes of  $\sim 4$  to 13 m (Figure 6). We note that cumulative  
 596 oblique slip magnitudes at Site 2 are likely underestimated, given that it was only pos-  
 597 sible to determine cumulative displacement across a portion of the mapped strands due  
 598 to limited exposure and preservation.

599 Our calculated vertical and oblique displacement magnitudes show that older de-  
 600 posits typically record greater amounts of displacement than younger deposits. Exam-  
 601 ples of this relationship can be observed in the comparison of vertical separation along  
 602 adjacent profiles at Sites 1 and 2 (Figure 10). At Site 1 (strand D, Figures 5, 10a) there  
 603 is 5.8 m of vertical separation across an offset interfluve developed in Qp1, the oldest off-  
 604 set deposit at the site, whereas the adjacent, younger abandoned channel shows only 4.7  
 605 m of vertical separation. A younger Qft2 fluvial terrace, which crosses adjacent fault strand  
 606 Ee, has even less vertical separation (2.3 m). Similarly, at Site 2, we find that the till-  
 607 mantled hillslope typically has larger vertical separation than channels incised into till.  
 608 For example, profile 28 at Site 2 in Qt shows 4.1 m of vertical separation across strand  
 609 Q, whereas profile 33 along a younger channel incised into Qt shows only 2.9 m of ver-  
 610 tical separation (Figures 6, 10b). Finally, we were able to expand this assessment of cu-  
 611 mulative displacement to a set of 23 interfluves and channels at Site 1 for which we are  
 612 able to reconstruct 3D displacement. These data show that older interfluves developed  
 613 in Qp1 consistently have  $\sim 4$  to 10 m more cumulative oblique displacement as compared  
 614 to young channels incised into Qp1 (Figure 10c).

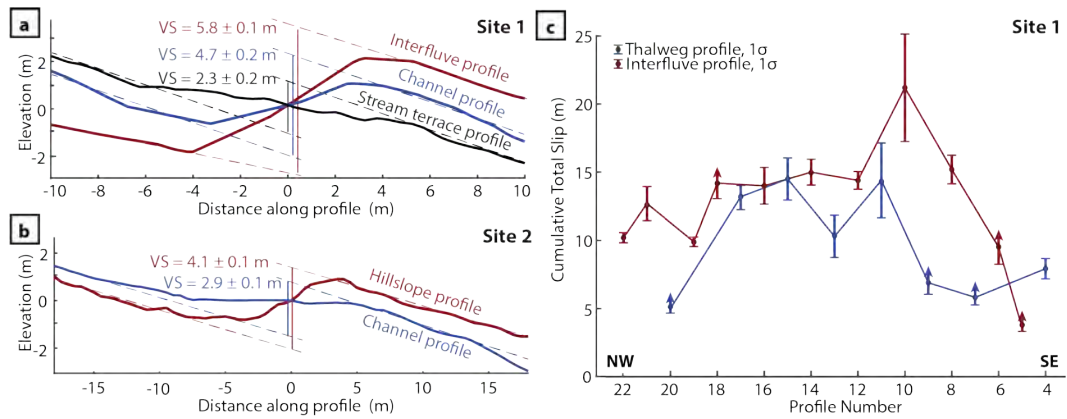


**Figure 10.** Topographic survey data showing differential magnitudes of fault offset in deposits of different ages. **A:** Example from Site 1D where there is the largest magnitude of vertical separation across an interfluvial developed in Qp1 (profile 10, strand D), intermediate magnitudes across a channel incised into Qp1 (profile 11, strand D, channel age correlative to deposit Qp2), and minimum magnitudes across a Holocene stream terrace (profile 3, strand Ee). **B:** Example from Site 2A where there is greater vertical separation across the till mantled hillslope (profile 28, Qt.), and smaller separation across a channel incised into till (profile 33, strand Q). **C:** Cumulative slip estimates from Site 1D profiles: cumulative slip across interfluvies (mean =  $12.7 \pm 4.4$  m) is greater than for thalwegs (mean =  $9.8 \pm 3.9$  m), suggesting interfluvies have experienced at least one more event than thalwegs. Arrows indicate minimum slip estimates in locations where displacements across one or more strands could not be reconstructed.

## 5 Discussion

### 5.1 Characteristics of the Quaternary-active BRF

The field data and observations provided in this paper provide unequivocal evidence that the scarps we identify along the southwestern flank of the Beaufort Range are tectonic in origin and are associated with an active Beaufort Range fault. Mapped scarps form en echelon steps, and parallel arrays exhibit geometries common in strike-slip fault systems and pull-apart basins (e.g., Hatem et al., 2017; van Wijk et al., 2017), and occur along several tens of kilometers of strike length. The magnitudes of displacement and total fault lengths are consistent with observed displacement-length scaling relationships for active faults in Cascadia (R. H. Styron & Sherrod, 2021), and globally (D. L. Wells & Coppersmith, 1994; Wesnousky, 2008).

The scarps are inconsistent with formation processes associated with gravitational failure, glacial, or anthropogenic processes, for several reasons. First, scarps are predominantly uphill-facing, and are associated with steep NE-dipping fault planes that produce “valley-side up” displacement. This sense of displacement is opposite to that predicted for landslide-related failures. Second, the scarps are quasi-linear and extend for several km along strike, whereas headscarps associated with landslides tend to produce curvilinear and discontinuous scarps with limited strike lengths. Third, the mapped scarps are inconsistent with formation by sackungen (McCalpin et al., 1999), which typically form sets of parallel scarps at range crests, rather than the en echelon scarps we observe near the base of the range (e.g., Figure 2b as compared to Figure 3c). Finally, our field observations also confirm that these scarps are not associated with roads, logging tracks, or other anthropogenic disturbances, nor are they associated with glacial scouring or glacially-streamlined deposits (see Supplemental Text S1).

Our data indicate that the BRF consists of a set of high-angle faults, with an average 60-88° NE dip, with local fault strand strikes ranging from  $\sim 270^\circ$  to  $320^\circ$ . While individual fault strands extend for several hundred m to several km, these strands collectively define a discontinuous network of scarps that we interpret to be the surficial expression of a single fault zone at depth. Such discontinuous fault scarp networks are common in strike-slip systems, especially in immature faults with little cumulative offset (e.g., Hatem et al., 2017), and have been observed along other forearc faults in northern Cascadia (e.g., Morell et al., 2017). The mapped network of BRF fault scarps identified in this study extends for  $\sim 40$  km from Port Alberni to Comox Lake (Figure 2b and 1). Ad-

ditional potential scarps visible in lidar DEMs occur along strike of the active BRF outside the map area, suggesting that the BRF may have a cumulative length that is >40 km (Figure 1). If all of the mapped scarps in this study are associated with a continuous subsurface fault network, then the BRF is one of the longest strike-length faults identified in northern Cascadia to date.

## 5.2 Kinematics of the BRF and relationship to inherited structures

Our field mapping and topographic survey data demonstrate that the active BRF is a transtensional structure that accommodates right-lateral oblique slip along a steeply NE-dipping fault zone (Figure 9). Three lines of evidence support this interpretation: 1) Field observations show consistent right-lateral offset of abandoned channels and interfluvial and net NE-side-down vertical displacement. 2) Slip vectors resolved by reconstructing piercing lines similarly indicate NE-side-down hanging wall motion, consistent with right-lateral transtensional slip on a steeply NE dipping fault (Figure 9). These kinematics are consistent with mapped fault scarp geometries that suggest formation during right-lateral transtension. For example, at Site 1 (Figures 5a, 8), there is an en echelon array of faults with opposing dips that is consistent with the map patterns expected for a right-lateral transtensional negative flower structure. 3) Pseudo focal mechanism inversion of slip vectors indicate that the BRF accommodates right-lateral transtension along a steeply NE dipping fault plane.

The NE-side-down slip sense we determine for the Quaternary-active BRF produces a “range-side down” sense of motion. This result suggests that the high elevations and steep topography associated with the southwestern flank of the Beaufort Range were not formed by transtensional slip along the active BRF. Instead, the steep range front may be the product of differential erosion of the softer Cretaceous Nanaimo Gp sediments that underlie the Alberni Valley, relative to the more resistant Karmutsen Fm basalts that underlie the range crest (Muller & Carson, 1969). Or, this may imply that the net range-side-down (NE-side down) motion integrated over 100s kyr to Myr across the active BRF may be small relative to the amount of Eocene NE-side-up thrust fault displacement. The small cumulative magnitude of NE-side-down motion could indicate that transtension across the BRF is a relatively young phenomenon, and has not accrued a large magnitude of vertical displacement.

679 Finally, our data suggest that active BRF strands do not appear to directly reoc-  
680 cupy inherited thrust fault planes. The presence of active BRF scarps in both the hang-  
681 ing wall and footwall of inherited thrust faults (Figure 4) suggest that there is not a strong  
682 inherited lithologic or mechanical control on the position of the active BRF at the sur-  
683 face. Furthermore, there is an apparent difference between the near-surface dip of the  
684 Quaternary-active BRF (70-90°) and that of the inherited Eocene Beaufort Range thrust  
685 fault (~45-70°). There are two possible explanations for this apparent dip discrepancy.  
686 First, these observations could imply that the subsurface projections of the active and  
687 Eocene faults may diverge at depth. Similar discrepancies between active and inherited  
688 fault geometries have been observed in the northern Cascadia forearc along the Leech  
689 River and North Olympic faults (Morell et al., 2017; G. Li et al., 2017; Nelson et al., 2017;  
690 Schermer et al., 2021). These data suggest that it is possible that the active BRF may  
691 reflect the formation of a new fault, more optimally oriented in the forearc stress field,  
692 rather than slip on an inherited bedrock structure. The second possibility is that the dip  
693 of the BRF is steep near the surface, but has a more gentle dip at depth, such that the  
694 active transtensional fault follows the Eocene thrust fault at depth. The geometry, kine-  
695 matics, and slip history of the active BRF therefore provide critical insight into the neo-  
696 tectonic stress and strain fields in the northern Cascadia forearc.

### 697 **5.3 Evidence for multiple surface-rupturing late Pleistocene to Holocene** 698 **earthquakes**

699 Our tectonogeomorphic mapping, topographic surveys of offset abandoned chan-  
700 nels and interfluves, and field observations of fault scarp morphology support the hypoth-  
701 esis that the BRF has hosted multiple earthquakes since the deglaciation of the Alberni  
702 Valley (~14-11 ka). The strongest evidence for multiple events comes from the differ-  
703 ential scarp heights and cumulative slip magnitudes calculated for offset landforms of dif-  
704 ferent ages at Sites 1 and 2 (Figure 10). At Site 1, interfluve crests developed in the older  
705 paraglacial unit Qp1 have greater vertical separation (~1 m) and greater cumulative oblique  
706 slip (~1-3 m) than abandoned channel thalwegs incised into that same unit. These aban-  
707 doned channels in turn have greater vertical separation (~2.4 m) than the displacement  
708 surveyed across a younger Qft2 fluvial terrace. The differential offset between interfluves,  
709 channels, and fluvial terraces indicates the occurrence of at least three events since the  
710 deposition of Qp1 at Site 1. At Site 2, differential scarp heights of ~2 m between those

711 developed in till-mantled hillslopes and younger channels incised into the hillslopes in-  
 712 dicate at least two surface-rupturing events have occurred at this site following the de-  
 713 position of Qt. Furthermore, if we make the simplifying assumption that a single event  
 714 produces  $\sim 1\text{-}3$  m of oblique slip, based on the average difference in cumulative oblique  
 715 displacement between interfluves and channels, these data suggest the BRF may have  
 716 hosted more than three events since  $\sim 11\text{-}14$  ka.

717 At Site 1, we can place broad constraints on the relative timing of slip events by  
 718 combining our estimates of deposit ages (Table 1; Figure 4c) with offset magnitudes (Ta-  
 719 ble S2; Figure 6). The timing of the first event is constrained by the observation that  
 720 older interfluves developed in Qp1 have more cumulative oblique offset than channels de-  
 721 veloped in Qp1. This observation indicates that at least one event must have occurred  
 722 more recently than the deposition of Qp1, which occurred after deglaciation ( $\sim 11\text{-}14$  ka),  
 723 but before the abandonment of channels incised into Qp1. The timing of channel aban-  
 724 donment is not directly dated, but our correlation of channel incision to the deposition  
 725 of Qp2 suggests channel abandonment occurred after the deposition of Qp2 (radiocar-  
 726 bon dated to  $\sim 6$  to 11 ka) and before the deposition of Qaf (radiocarbon dated to  $\sim 3\text{-}$   
 727 6 ka). Therefore, the first event(s) likely occurred after  $\sim 11\text{-}14$  ka, but before  $\sim 3\text{-}6$  ka.  
 728 The timing of the second event is constrained by the difference in offset between chan-  
 729 nels and inset Qft2 terraces. This difference requires one or more events to have occurred  
 730 after channel abandonment (which we infer occurred after 6-11 ka), but before the for-  
 731 mation of the Qft2 terrace (radiocarbon dated to  $< \sim 4$  ka). The occurrence of a third  
 732 event is supported by the  $\sim 1.5$  m of vertical offset of the Qft2 terrace. Therefore, the  
 733 most recent event must have occurred after the deposition of the Qft2 terrace (since  $\sim 4$   
 734 ka).

735 These data suggest that the BRF has experienced at least three events over the late  
 736 Pleistocene to late Holocene. The persistence of right-lateral transtensional deformation  
 737 along the BRF for several thousand years after the retreat of glaciers from the Alburni  
 738 Valley indicates that deformation cannot be attributed solely to changes in crustal loads  
 739 and stresses due to glacial unloading and viscoelastic relaxation of the crust and man-  
 740 tle (e.g., Anderson et al., 1989; Craig et al., 2016; Davenport et al., 1989; Lagerbäck, 1990;  
 741 Mörner, 1991; Muir-Wood, 2000; Jarman & Ballantyne, 2002; van Loon et al., 2016). Such  
 742 “glacially-induced” earthquakes typically occur during or within a few kyr of glacial re-  
 743 treat, when changes in ice loads and crustal stresses from the viscoelastic rebound are

744 greatest (Steffen et al., 2014). While our data do not constrain the precise timing of the  
745 first event(s), and cannot rule out that early events on the BRF were impacted by glacial  
746 unloading, they do indicate earthquakes have occurred in the middle to late Holocene,  
747 well after the largest stress changes due to glacial loading would have occurred. Addi-  
748 tionally, we note that glacial unloading typically reduces vertical stress, and given that  
749 our slip data indicate the BRF accommodates transtension, such unloading would re-  
750 duce the deviatoric stress making failure less likely. Overall, the persistence of right-lateral  
751 transtensional events throughout the Holocene suggests that tectonic forces are the prin-  
752 cipal drivers of deformation, and any glacial impacts are secondary.

753 Our estimates of displacement per event, and measurements of the total length of  
754 the active BRF from mapped or inferred fault scarps, allow us to estimate the magni-  
755 tude of paleo-earthquakes at these sites using displacement scaling relationships. An es-  
756 timated  $\sim 1\text{-}3$  m of displacement per event suggests that the BRF could have hosted  $M_W$   
757 6.9 to 7.2 events (D. L. Wells & Coppersmith, 1994). These magnitudes are similar to  
758 those determined based on our total mapped fault length of 35 to  $>40$  km, which sug-  
759 gests  $M_W$  6.8 to  $>7.0$  events (D. L. Wells & Coppersmith, 1994; Wesnousky, 2008). These  
760 earthquake magnitudes are similar in scale to the  $M$  7.3 magnitude calculated for the  
761 1946 Vancouver Island earthquake, which caused significant damage, including to tele-  
762 phone wires, underwater telegraph cables, and the hospital in Port Alberni, BC (Hodgson,  
763 1946). An earthquake of a similar magnitude today would pose significant hazard not  
764 only to Port Alberni, but also to the nearby communities of Nanaimo, Parksville, Qualicum  
765 Beach, and Courtenay (Figure 2a). Failure of dams on Comox Lake and Elsie Lake could  
766 lead to flooding of communities downstream (Figure 2b), as well as impacts on power  
767 availability, as nearby power stations supply 11% of the electricity generated on Vancou-  
768 ver Island (BC Hydro, n.d.).

#### 769 **5.4 Estimate of Late Pleistocene to Holocene slip rates**

770 Estimation of fault slip rates yields important information relevant to understand-  
771 ing how strain is partitioned among faults, and they represent primary data used in seis-  
772 mic hazard analyses (Morell et al., 2020). Ideally, slip rates are calculated when at least  
773 two precise earthquake ages and the displacement associated with the bracketed event  
774 are known (e.g., a closed interval slip rate, DuRoss et al., 2020) and estimated over a time  
775 period spanning more than 5 earthquakes (R. Styron, 2019). In the absence of precise

776 earthquake ages, a geomorphic slip rate can be estimated that affords an estimate of the  
777 slip rate that has accrued since the development of the geomorphic feature, using esti-  
778 mates of the date of the landform and displacement data recorded in the geomorphic fea-  
779 ture. However, such an open-interval slip rate can be biased because the age of the ge-  
780 omorphic feature can differ from the age of the earthquake that deformed the feature.

781 On the BRF, we currently do not have precise earthquake ages, and we do not know  
782 the displacement between earthquakes with precision. However, we nonetheless make broad  
783 estimates of slip rate based on the known ages and displacements between known events.  
784 The cumulative displacement of different deposits, their depositional ages, and our es-  
785 timates of event timing, place bounds on fault slip rates for the active BRF. Both open-  
786 ended and closed interval approaches at Site 1 yield slip rates for the BRF that range  
787 from  $\sim 0.5$  to  $\sim 2$  mm/yr. The open-ended approach yields a rate of  $\sim 0.7$ - $1.3$  mm/yr, based  
788 on the  $\sim 10$  to  $15$  m of cumulative oblique slip across all mapped fault strands and an  
789 estimated deglaciation age of  $\sim 11.5$ - $13.6$  ka. There is only one reliable closed interval  
790 calculation that can be made given the available offset data and uncertainties in event  
791 timing. This interval calculation uses the  $\sim 8$ - $9$  m cumulative displacement of the chan-  
792 nels at Site 1, and the difference in age between the Qft2 terrace and the interfluves at  
793 Site 1, which could range from  $\sim 3.5$  to  $13.6$  kyr. This closed interval spans at least two  
794 events, and yields a slip rate estimate of  $0.6$ - $2.6$  mm/yr. Given the uncertainties in the  
795 ages of events and displacement magnitudes in this closed interval calculation, we pre-  
796 fer the more conservative open-ended rate of  $0.7$ - $1.3$  mm/yr.

797 These data demonstrate that, even at the lower bound of uncertainty, the Beau-  
798 fort Range fault is one of the fastest-slipping Quaternary faults in the northern Casca-  
799 dia forearc. Our slip rate estimates of  $\sim 0.5$  to  $\sim 2$  mm/yr indicate that the BRF has a  
800 higher slip rate than the nearby LRF ( $0.2$ - $0.3$  mm/yr; Morell et al., 2017, 2018) and Darrington-  
801 Devils Mountain fault zone DMF ( $0.14 \pm 0.1$  mm/yr; Personius et al., 2014), and a sim-  
802 ilar slip rate to the NOFZ ( $1.3$ - $2.3$  mm/yr, 3-5 post-glacial earthquakes; Schermer et al.,  
803 2021). These data suggest that the BRF is a major crustal structure that accommodates  
804 permanent deformation in the northern Cascadia forearc.

## 5.5 Comparison of the 1946 Vancouver Island earthquake kinematics with slip on the BRF

The field data reported here cannot constrain the timing of the most recent event along the active BRF beyond that it occurred after  $\sim 3.5$  ka, and therefore cannot directly test whether the 1946 event ruptured along the BRF within our field area. However, our data from the Holocene BRF share striking similarities to the kinematics, spatial distribution, and fault plane solutions for the 1946 event.

The pseudo-focal mechanism solutions for the BRF determined from kinematic inversions of fault slip have similar slip planes, slip vectors, and P- and T-axes as those determined for the 1946 Vancouver Island earthquake (Figure 9). Focal mechanism solutions for the 1946 earthquake (Rogers & Hasegawa, 1978) have NW-SE striking nodal planes with strikes of  $319\text{-}332^\circ$  and dips of  $66\text{-}79^\circ$ , and SW-NE striking nodal planes with strikes of  $222\text{-}233^\circ$  and dips of  $36\text{-}85^\circ$  (Figure 9f, Table S3). These nodal plane attitudes are strikingly similar to the nodal planes of the pseudo-focal mechanisms solutions derived from fault slip vectors along the active BRF (Figure 9). The NW-SE nodal plane of the focal mechanism preferred by Rogers and Hasegawa (1978) of  $319/79$  NE is sub-parallel to our calculated attitude of the active BRF of  $\sim 270\text{-}320/\sim 75$ , and the predicted slip vectors associated with the NW-SE striking nodal planes for the 1946 earthquake have trends ranging from  $114$  to  $143^\circ$ , and plunges ranging from  $05^\circ$  to  $55^\circ$ —similar slip vector orientations to those determined from offset piercing lines along the active BRF. Finally, the stress axes determined for the 1946 focal mechanism solutions have moderately plunging, southerly trending P-axes and sub-horizontal T-axes with trends similar to those determined for the active BRF (Figure 9).

The fault slip vectors and transtensional pseudo-focal mechanisms that we determine for the BRF are also similar to fault plane inversions based on geodetic motions associated with the 1946 earthquake (Slawson & Savage, 1979). Repeat surveys of topographic benchmarks across the Beaufort Range at the latitude of the earthquake epicenter ( $\sim 49.45^\circ$  N) suggest right-lateral oblique slip on a steeply ( $70^\circ$ ) NE-dipping fault plane that extended for 60 km along strike (Slawson & Savage, 1979). Our mapped Sites 1 and 2 along the BRF therefore lie within the modeled event rupture area, and the fault plane dip is similar to the  $60\text{-}88^\circ$  NE dip we determine for the BRF. In addition, slip inversions for the 1946 event fault planes indicate the crustal displacements are best reproduced by  $\sim 1$  m of right-lateral and  $\sim 2$  m dip slip, along 60 km fault length paral-

838 lel to the BRF. Therefore, both the relative ratio of strike slip to dip slip ( $\sim 0.5:1$ ) and  
 839 the estimated slip per event ( $\sim 1\text{-}2$  m) modeled for the 1946 event are similar to our slip  
 840 ratios of 0.3-1.5:1 (strike slip to dip slip) and estimates of  $\sim 1\text{-}3$  m of oblique slip per BRF  
 841 event.

842 These data collectively indicate that the Holocene slip observed along the active  
 843 BRF is kinematically and spatially compatible with the slip inferred for the 1946 Van-  
 844 couver Island earthquake. These correlations suggest that, if the 1946 event failed along  
 845 a NW-SE striking, steeply NE-dipping plane, as suggested by Rogers and Hasegawa (1978)  
 846 and Slawson and Savage (1979), the BRF is a likely candidate for hosting this event. Our  
 847 estimated age of the most recent event of  $<3\text{-}4$  ka allows for this possibility. Furthermore,  
 848 our field offset data provide evidence that the active BRF has hosted at least 3 earth-  
 849 quakes since the late Pleistocene, each with slip that is compatible with that modelled  
 850 for the NW-SE striking nodal plane for the 1946 event. These observations suggest then  
 851 that the BRF hosted multiple 1946-like events over the late Pleistocene to Holocene.

## 852 **5.6 Implications for forearc strain accommodation**

853 These results have several key implications for the long-term permanent strain ac-  
 854 cumulation in the northern Cascadia forearc. First, our field data and kinematic inver-  
 855 sions for the active BRF indicate that this portion of the Cascadia forearc has experi-  
 856 enced right-lateral transtension over the past  $\sim 11\text{-}14$  ka. In addition, the similarity be-  
 857 tween the fault kinematics integrated over multiple paleoseismic events spanning the late  
 858 Pleistocene to Holocene and the 1946 Vancouver Island earthquake suggests that these  
 859 transtensional kinematics are representative of the local upper plate deformation field  
 860 over decadal to millennial time scales. If true, these time scales would span multiple up-  
 861 per plate fault seismic cycles, which likely have recurrence intervals of 1000s of years (e.g.,  
 862 Morell et al., 2018; Schermer et al., 2021), and multiple subduction interface megath-  
 863 rust seismic cycles, which have recurrence periods of  $\sim 390\text{-}540$  years (e.g., Walton et al.,  
 864 2021).

865 Second, the slip kinematic inversions for the active BRF suggest that the P- and  
 866 T-axes inverted for long-term (late-Pleistocene to present) slip are consistent with re-  
 867 gional stress patterns derived from historical seismicity (Figure 2a; Balfour et al., 2011).  
 868 We find that the trends and plunges of P- and T-axes determined for the BRF are within  
 869  $\sim 20\text{-}40^\circ$  of the P- and T-axes determined for the 1946 Vancouver Island earthquake and

870 from inversions determined from nearby upper plate seismicity (Balfour et al., 2011). Sev-  
871 eral studies have suggested that variations in trench-perpendicular tractions during the  
872 megathrust seismic cycle can cause inversions in principal stress orientations in the over-  
873 riding plate, such that forearc fault slip sense can vary as a function of the megathrust  
874 seismic cycle (e.g., Wang et al., 1995; Loveless et al., 2010; Regalla et al., 2017). How-  
875 ever, the consistency of P- and T-axes determined from historical earthquakes and from  
876 paleoseismic slip suggests that BRF kinematics have not changed drastically over Holocene  
877 time scales. These data suggest that there is some level of consistency in the deforma-  
878 tion field associated with short-term (decadal) upper plate seismicity and long-term (kyr-  
879 scale) fault slip, and a potentially similar temporal consistency in the upper plate stress  
880 field.

881 Third, a comparison between these BRF fault kinematics to those determined for  
882 other active faults in the northern Cascadia forearc, suggests that there may be a spa-  
883 tial transition from a forearc deformation field promoting right-lateral transpression near  
884 the Olympic Mountains and on southernmost Vancouver Island, to one promoting right-  
885 lateral transtension in the northern Cascadia forearc on central Vancouver Island. Specif-  
886 ically, the North Olympic fault zone, the Darrington-Devils Mountain fault, the South-  
887 ern Whidbey Island fault, the Leech River fault, and the XEOLXELEK-Elk lake fault  
888 appear to be accommodating right-lateral slip and compression, as determined by earth-  
889 quake focal mechanisms and paleoseismic data (Sherrod et al., 2008; Personius et al., 2014;  
890 Schermer et al., 2021; Morell et al., 2018; Harrichhausen et al., 2021, 2023). In contrast,  
891 at the latitude of central Vancouver Island, the BRF appears to be accommodating right-  
892 lateral transtension, as determined by kinematic inversions of offset geomorphic pierc-  
893 ing lines across the BRF.

894 This observation suggests that there may be a change in the upper plate strain field  
895 from one favoring transpression on faults near the Olympic Mountains to one favoring  
896 transtension on faults in northern Cascadia, around the latitude of 48.5-49° N. This change  
897 in strain field may be related to spatial variations in principal stress orientations and mag-  
898 nitudes in the upper plate that locally promote transtension along the BRF. While the  
899 data presented here are not sufficient to determine the causes of this potential change  
900 in the upper plate deformation field, there are several possibilities, including oroclinal  
901 bending (Johnston & Acton, 2003; Finley et al., 2019; Harrichhausen et al., 2021), spa-  
902 tial changes in plate tractions, convergence rate, or obliquity (R. E. Wells et al., 1998;

903 Wang, 2000; McCaffrey et al., 2013; S. Li et al., 2018), or the ‘escape’ of forearc crustal  
904 blocks related to north-directed shear from southern Cascadia (Nelson et al., 2017). The  
905 consistency of fault kinematics and P- and T-axes calculated near the BRF from both  
906 seismic and paleoseismic data suggest that a deformation field favoring local right-lateral  
907 transtension has persisted over both decadal and millennial timescales.

## 908 **6 Conclusions**

909 We provide the first geologic field evidence that the Beaufort Range fault is a seis-  
910 mogenic fault, and demonstrate that it actively accommodates right-lateral transtension  
911 within the northern Cascadia forearc of central Vancouver Island. Field mapping and  
912 topographic surveys document >35-40 km of northwest-striking, primarily northeast-dipping  
913 fault strands along the southwestern flank of the Beaufort Range. These scarps occur  
914 in discontinuous, en echelon and parallel sets and offset late Pleistocene to Holocene glacial,  
915 paraglacial, and post-glacial deposits. We observe an increase in scarp height and total  
916 offset with increasing unit age that provides evidence for at least three surface-rupturing  
917 earthquakes on the BRF since ~13.6-11 ka, the most recent of which occurred in the past  
918 ~3-4 kyr. Slip magnitudes reconstructed from offset piercing lines, total fault length, and  
919 the ages of offset deposits suggest that the BRF is capable of hosting earthquakes of  $M_W$   
920 6.5-7.5, and has a late Pleistocene to Holocene slip rate of 0.5 to 2 mm/yr. Thus the BRF  
921 is a major forearc fault accommodating deformation in the northern Cascadia subduc-  
922 tion zone, and poses significant hazard to communities and infrastructure on Vancou-  
923 ver Island.

924 Notably, kinematic slip inversions of geomorphic piercing lines offset by the BRF  
925 yield transtensional pseudo-focal mechanisms, fault geometries, slip vectors, and P- and  
926 T-axes that are remarkably similar to those determined for the 1946 Vancouver Island  
927 earthquake. These data suggest that the BRF is a candidate structure to have hosted  
928 this event. The consistency of right-lateral transtensional slip kinematics between the  
929 1946 earthquake and late Pleistocene to Holocene slip on the BRF suggests that this por-  
930 tion of the northern Cascadia forearc has accommodated regional transtension over decadal  
931 to millennial time scales, spanning multiple earthquake cycles.

## 932 **7 Open Research**

933 New data produced in this study:

934 Data collected and analyzed in this manuscript are available in a Dryad Data Repos-  
 935 itory (Lynch et al., 2023) at  
 936 <https://datadryad.org/stash/share/Ui8KejoZgz41xs10ZUxfCQV2Nea3JsVwQoTz9DZ1iho>.

937 The repository contains the following data:

- 938 1. Text files containing raw field data (x,y,elevation) of surveyed offset landforms
- 939 2. Text files containing raw field data (x,y,elevation) of fault midpoint locations
- 940 3. R script for calculating 3D fault plane geometry
- 941 4. R script for calculating 3D offsets of linear piercing lines across a dipping fault

942 Previously published data and programs used in this study:

- 943 1. The USGS Quaternary faults and folds database used for Figure 1 is available at  
 944 <https://www.usgs.gov/programs/earthquake-hazards/faults>.
- 945 2. The BC Geological Survey (BCGS) bedrock geology map used for Figures 2a, 4,  
 946 and Figure 1 is available at [https://www2.gov.bc.ca/gov/content/industry/  
 947 mineral-exploration-mining/british-columbia-geological-survey/geology/  
 948 bcdigitalgeology](https://www2.gov.bc.ca/gov/content/industry/mineral-exploration-mining/british-columbia-geological-survey/geology/bcdigitalgeology).
- 949 3. The OxCal program v. 4.4 by C. Bronk Ramsey used for radiocarbon calibration  
 950 is available at <https://c14.arch.ox.ac.uk/oxcal/OxCal.html>.
- 951 4. The R. Allmendinger FaultKin 7.6 program used for plotting and analyzing fault  
 952 plane and slip vector data in Figure 9 is available at [http://www.geo.cornell  
 953 .edu/geology/faculty/RWA/programs/faultkin.html](http://www.geo.cornell.edu/geology/faculty/RWA/programs/faultkin.html).
- 954 5. The OSX Stereonet 9.9.4 program used for plotting bedrock fault planes and slick-  
 955 enlines in Figure 7 is available at [http://www.geo.cornell.edu/geology/faculty/  
 956 RWA/programs/stereonet.html](http://www.geo.cornell.edu/geology/faculty/RWA/programs/stereonet.html).

## 957 **Acknowledgments**

958 This work was conducted on the traditional territory of the Hupačasath̓, K'ómoks, and  
 959 ćišaaʔath̓ people, and we acknowledge their historical relationships with the land that  
 960 continue to this day. Funding for this project was supported by NSF EAR Tectonics 1756834/  
 961 2004684 to Regalla and 1756943 to Morell, by the Boston University Department of Earth  
 962 and Environmental Sciences, and the Northern Arizona University Duebendorfer-Barnes  
 963 Structure Endowment. We would like to thank Todd Thompson, TimberWest, and Is-  
 964 land Timberlands for land access, and Mosaic/Island Timberlands/TimberWest for pro-

965 viding lidar ground return data, as well as Edwin Nissen and the University of Victo-  
 966 ria School of Earth and Ocean Sciences for discussion of local tectonics and help with  
 967 field logistics. We would also like to acknowledge the late Vic Levson for help with un-  
 968 derstanding glacial systems of Vancouver Island, and Johanna Fischi and Tatum McLeod  
 969 for assistance in the field.

## 970 References

- 971 AGI. (2003). *Global GIS: Volcanoes of the world*.  
 972 <https://earthworks.stanford.edu/catalog/harvard-glb-volc>.
- 973 Alley, N. F., & Chatwin, S. C. (1979). Late Pleistocene history and geomorphology,  
 974 southwestern Vancouver Island, British Columbia. *Canadian Journal of Earth*  
 975 *Sciences*, *16*(9), 1645–1657.
- 976 Allmendinger, R. W., Cardozo, N., & Fisher, D. M. (2012). *Structural geology algo-*  
 977 *rithms: Vectors and tensors in structural geology*. Cambridge University Press.
- 978 Anderson, W. A., Borns, H. W., Kelley, J. T., & Thompson, W. B. (1989). Neotec-  
 979 tonic Activity in Coastal Maine. *Maine Geological Survey*, 195–212.
- 980 Angelier, J., & Mechler, P. (1977, January). Sur une methode graphique de  
 981 recherche des contraintes principales egalement utilisables en tectonique et en  
 982 seismologie : La methode des diedres droits. *Bulletin de la Société Géologique*  
 983 *de France*, *S7-XIX*(6), 1309–1318.
- 984 Balfour, N. J., Cassidy, J. F., Dosso, S. E., & Mazzotti, S. (2011). Mapping crustal  
 985 stress and strain in southwest British Columbia. *Journal of Geophysical Re-*  
 986 *search: Solid Earth*, *116*(3), 1–11.
- 987 Ballantyne, C. K. (2002). A general model of paraglacial landscape response. *The*  
 988 *Holocene*, *12*, 371–376.
- 989 Ballantyne, C. K., & Benn, D. I. (1996). Paraglacial slope adjustment during re-  
 990 cent deglaciation and its implications for slope evolution in formerly glaciated  
 991 environments. In *Advances in Hillslope Processes* (Vol. 2, pp. 1173–1195).
- 992 BC Hydro. (n.d.). *Our facilities: Vancouver Island*.  
 993 [https://www.bchydro.com/energy-in-bc/operations/our-facilities/vancouver-](https://www.bchydro.com/energy-in-bc/operations/our-facilities/vancouver-island.html)  
 994 [island.html](https://www.bchydro.com/energy-in-bc/operations/our-facilities/vancouver-island.html).
- 995 Blaise, B., Clague, J. J., & Mathewes, R. W. (1990, November). Time of Maxi-  
 996 mum Late Wisconsin Glaciation, West Coast of Canada. *Quaternary Research*,

- 997           34(3), 282–295.
- 998   Brocher, T. M., Parsons, T., Blakely, R. J., Christensen, N. I., Fisher, M. A., &  
999       Wells, R. E. (2001). Upper crustal structure in Puget Lowland, Washington:  
1000       Results from the 1998 Seismic Hazards Investigation in Puget Sound. *Journal*  
1001       *of Geophysical Research: Solid Earth*, 106(B7), 13541–13564.
- 1002   Brodzikowski, K., & van Loon, A. J. (1987). A systematic classification of glacial  
1003       and periglacial environments, facies and deposits. *Earth Science Reviews*,  
1004       24(5), 297–381.
- 1005   Bronk Ramsey, C. (1995). Radiocarbon Calibration and Analysis of Stratigraphy:  
1006       The OxCal Program. *Radiocarbon*, 37(2), 425–430.
- 1007   Bronk Ramsey, C. (2021). *OxCal Program, Version 4.4*. Oxford Radiocarbon Accel-  
1008       erator Unit, University of Oxford.
- 1009   Clague, J. J. (1980). Late Quaternary geology and geochronology of British  
1010       Columbia: Part 1: Radiocarbon dates. *Geological Survey of Canada Paper*,  
1011       80–13.
- 1012   Clague, J. J. (1994). Quaternary stratigraphy and history of south-coastal British  
1013       Columbia. *Geological Survey of Canada Bulletin*, 481, 181–192.
- 1014   Clague, J. J. (1996). Paleoseismology and seismic hazards, southwestern British  
1015       Columbia. *Geological Survey of Canada Bulletin*, 494.
- 1016   Clague, J. J., & James, T. S. (2002). History and isostatic effects of the last ice  
1017       sheet in southern British Columbia. *Quaternary Science Reviews*, 21, 71–87.
- 1018   Clowes, R. M., Yorath, C. J., & Hyndman, R. D. (1987). Reflection mapping across  
1019       the convergent margin of western Canada. *Geophysical Journal of the Royal*  
1020       *Astronomical Society*, 89(1), 79–84.
- 1021   Craig, T. J., Calais, E., Fleitout, L., Bollinger, L., & Scotti, O. (2016). Evidence for  
1022       the release of long-term tectonic strain stored in continental interiors through  
1023       intraplate earthquakes. *Geophysical Research Letters*, 43(13), 6826–6836.
- 1024   Cui, Y., Miller, D., Schiarizza, P., & Diakow, L. (2017). *British Columbia digital*  
1025       *geology* (Tech. Rep. No. 2017-8). British Columbia Ministry of Energy, Mines  
1026       and Petroleum Resources.
- 1027   Davenport, C., Ringrose, P., Becker, A., Hancock, P., & Fenton, C. (1989). Geologi-  
1028       cal Investigations of Late and Post Glacial Earthquake Activity in Scotland. In  
1029       S. Gregersen & P. Basham (Eds.), *Earthquakes at North-Atlantic Passive Mar-*

- 1030 *gins: Neotectonics and Postglacial Rebound* (pp. 175–194). Kluwer Academic  
1031 Publishers.
- 1032 Delano, J. E., Amos, C. B., Loveless, J. P., Rittenour, T. M., Sherrod, B. L., &  
1033 Lynch, E. M. (2017). Influence of the megathrust earthquake cycle on upper-  
1034 plate deformation in the Cascadia forearc of Washington State, USA. *Geology*,  
1035 *45*(11), 1051–1054.
- 1036 DuRoss, C. B., Gold, R. D., Briggs, R. W., Delano, J. E., Ostenaar, D. A., Zellman,  
1037 M. S., . . . Mahan, S. A. (2020, July). Holocene earthquake history and slip  
1038 rate of the southern Teton fault, Wyoming, USA. *GSA Bulletin*, *132*(7-8),  
1039 1566–1586.
- 1040 Easterbrook, D. J. (1992). Advance and retreat of Cordilleran ice sheets in Washing-  
1041 ton, U.S.A. *Géographie Physique et Quaternaire*, *46*(October), 51–68.
- 1042 England, T., & Calon, T. J. (1991). The Cowichan fold and thrust system, Vancou-  
1043 ver Island, southwestern British Columbia. *Geological Society of America Bul-  
1044 letin*, *103*(3), 336–362.
- 1045 England, T. D. J. (1990). *Late Cretaceous to Paleogene evolution of the Georgia  
1046 Basin, southwestern British Columbia* (Unpublished doctoral dissertation).  
1047 University of British Columbia.
- 1048 England, T. D. J., Currie, L. D., Massey, N. W., Roden-Tice, M. K., & Miller, D. S.  
1049 (1997). Apatite fission-track dating of the Cowichan fold and thrust system,  
1050 southern Vancouver Island, British Columbia. *Canadian Journal of Earth  
1051 Sciences*, *34*(5), 635–645.
- 1052 Eyles, N., Boyce, J. I., & Barendregt, R. W. (1999, February). Hummocky moraine:  
1053 Sedimentary record of stagnant Laurentide Ice Sheet lobes resting on soft beds.  
1054 *Sedimentary Geology*, *123*(3-4), 163–174.
- 1055 Finley, T., Morell, K. D., Leonard, L., Regalla, C., Johnston, S. T., & Zhang, W.  
1056 (2019). Ongoing oroclinal bending on the Cascadia forearc margin and its  
1057 relation to concave-outboard plate margin geometry. *Geology*, *47*(2), 155–158.
- 1058 Fyles, J. G. (1963). Surficial geology of Horne Lake and Parksville map-areas, Van-  
1059 couver Island, British Columbia. *Geological Survey of Canada Memoir*, *318*,  
1060 142.
- 1061 Geological Survey, U. (n.d.). *Quaternary fault and fold database for the United  
1062 States*.

- 1063 Goldfinger, C., Kulm, L. D., Yeats, R. S., Appelgate, B., Mackay, M. E., & Moore,  
 1064 G. F. (1992). Transverse structural trends along the Oregon convergent  
 1065 margin: Implications for Cascadia earthquake potential and crustal rotations.  
 1066 *Geology*, *20*(2), 141–144.
- 1067 Graham, A. (2017). *Geometry, kinematics, and Quaternary activity of the Leech*  
 1068 *River fault zone, southern Vancouver Island, British Columbia, Canada* (MSc  
 1069 Thesis). University of Victoria.
- 1070 Halsted, E. C. (1968). The Cowichan Ice tongue, Vancouver Island. *Canadian Jour-*  
 1071 *nal of Earth Sciences*, *5*, 1409–1415.
- 1072 Harrichhausen, N., Finley, T., Morell, K. D., Regalla, C. A., Bennett, S. E. K.,  
 1073 Leonard, L. J., ... Sethanant, I. (2023). Paleoseismic study of the XEOLX-  
 1074 ELEK–Elk Lake fault: A newly identified Holocene fault in the northern Cas-  
 1075 cadia forearc near Victoria, British Columbia, Canada. In *11th International*  
 1076 *INQUA Meeting on Paleoseismology, Active Tectonics and Archeoseismology*  
 1077 (Vols. 90–93, p. 4). France.
- 1078 Harrichhausen, N., Morell, K. D., Regalla, C., Bennett, S. E. K., Leonard, L. J.,  
 1079 Lynch, E. M., & Nissen, E. (2021, April). Paleoseismic Trenching Reveals  
 1080 Late Quaternary Kinematics of the Leech River Fault: Implications for Fore-  
 1081 arc Strain Accumulation in Northern Cascadia. *Bulletin of the Seismological*  
 1082 *Society of America*, *111*(2), 1110–1138.
- 1083 Hatem, A. E., Cooke, M. L., & Toeneboehn, K. (2017). Strain localization and  
 1084 evolving kinematic efficiency of initiating strike-slip faults within wet kaolin  
 1085 experiments. *Journal of Structural Geology*, *101*, 96–108.
- 1086 Hayes, G. P., Moore, G. L., Portner, D. E., Hearne, M., Flamme, H., Furtney, M.,  
 1087 & Smoczyk, G. M. (2018). Slab2, a comprehensive subduction zone geometry  
 1088 model. *Science*, *362*(October), 58–61.
- 1089 Herman, M. W., & Govers, R. (2020). Stress evolution during the megathrust earth-  
 1090 quake cycle and its role in triggering extensional deformation in subduction  
 1091 zones. *Earth and Planetary Science Letters*, *544*.
- 1092 Hodgson, E. (1946). British Columbia Earthquake June 23rd, 1946. *The Journal of*  
 1093 *The Royal Astronomical Society of Canada*, *40*(8), 285–319.
- 1094 Horst, A. E., Streig, A. R., Wells, R. E., & Bershaw, J. (2021). Multiple Holocene  
 1095 earthquakes on the Gales Creek fault, northwest Oregon fore-arc. *Bulletin of*

- 1096            *the Seismological Society of America*, 111(1), 476–489.
- 1097 Huang, M.-H., Morell, K. D., Duvall, A., Gallen, S. F., & Hilley, G. E.
- 1098            (2022).            *Exploring Subduction Zone Geohazards on Land and at Sea*.
- 1099            [http://eos.org/features/exploring-subduction-zone-geohazards-on-land-and-](http://eos.org/features/exploring-subduction-zone-geohazards-on-land-and-at-sea)
- 1100            [at-sea](http://eos.org/features/exploring-subduction-zone-geohazards-on-land-and-at-sea).
- 1101 Jarman, D., & Ballantyne, C. K. (2002, March). Beinn Fhada, Kintail: An Example
- 1102            of Large-scale Paraglacial Rock Slope Deformation. *Scottish Geographical Jour-*
- 1103            *nal*, 118(1), 59.
- 1104 Johnston, S. T., & Acton, S.            (2003).            The Eocene Southern Vancouver Island
- 1105            Orocline—a response to seamount accretion and the cause of fold-and-thrust
- 1106            belt and extensional basin formation. *Tectonophysics*, 365(1-4), 165–183.
- 1107 Kelsey, H. M., Sherrod, B. L., Nelson, A. R., & Brocher, T. M.            (2008).            Earth-
- 1108            quakes generated from bedding plane-parallel reverse faults above an active
- 1109            wedge thrust, Seattle fault zone. *Bulletin of the Geological Society of America*,
- 1110            120(11-12), 1581–1597.
- 1111 Kreemer, C., Blewitt, G., & Klein, E. C.            (2014, August).            A geodetic plate motion
- 1112            and Global Strain Rate Model. *Geochemistry, Geophysics, Geosystems*, 15(10),
- 1113            3849–3889.
- 1114 Lagerbäck, R.            (1990, December).            Late Quaternary faulting and-paleoseismicity
- 1115            in northern Fennoscandia, with particular reference to the Lansjärv area,
- 1116            northern Sweden.            *Geologiska Föreningen i Stockholm Förhandlingar*, 112(4),
- 1117            333–354.
- 1118 Lamontagne, M., Halchuk, S., Cassidy, J. F., & Rogers, G. C.            (2018).            *Significant*
- 1119            *Canadian earthquakes 1600-2017* (Tech. Rep. No. 8285).
- 1120 Lane, E.            (1947).            Report of the subcommittee on sediment terminology. *Transac-*
- 1121            *tions, American Geophysical Union*, 28, 936-938.
- 1122 Li, G., Liu, Y., Regalla, C., & Morell, K. D.            (2017).            Seismicity relocation and fault
- 1123            structure near the Leech River Fault Zone, southern Vancouver Island. , 4–8.
- 1124 Li, S., Wang, K., Wang, Y., Jiang, Y., & Dosso, S. E.            (2018).            Geodetically In-
- 1125            ferred Locking State of the Cascadia Megathrust Based on a Viscoelastic Earth
- 1126            Model. *Journal of Geophysical Research: Solid Earth*, 123(9), 8056–8072.
- 1127 Li, Z., Bruhn, R. L., Pavlis, T. L., Vorkink, M., & Zeng, Z.            (2010).            Origin of
- 1128            sacking uphill-facing scarps in the Saint Elias orogen, Alaska: LIDAR data vi-

- 1129 sualization and stress modeling. *Bulletin of the Geological Society of America*,  
 1130 *122*(9-10), 1585–1589.
- 1131 Liberty, L. M., Hemphill-Haley, M. A., & Madin, I. P. (2003, June). The Port-  
 1132 land Hills Fault: Uncovering a hidden fault in Portland, Oregon using high-  
 1133 resolution geophysical methods. *Tectonophysics*, *368*(1-4), 89–103.
- 1134 Loveless, J. P., Allmendinger, R. W., Pritchard, M. E., & González, G. (2010). Nor-  
 1135 mal and reverse faulting driven by the subduction zone earthquake cycle in the  
 1136 northern Chilean fore arc. *Tectonics*, *29*(2), 1–16.
- 1137 Lynch, E. M., Regalla, C., Morell, K. D., Harrichhausen, N., & Leonard, L. J.  
 1138 (2023). *Three-dimensional offsets of geomorphic piercing lines displaced by*  
 1139 *the Quaternary-active Beaufort Range fault, northern Cascadia forearc, BC,*  
 1140 *Canada* [Data set].
- 1141 Marrett, R., & Allmendinger, R. W. (1990). Kinematic analysis of fault-slip data.  
 1142 *Journal of Structural Geology*, *12*, 973–986.
- 1143 Mathews, W. H. (1979). Landslides of central Vancouver Island and the 1946 earth-  
 1144 quake. *Bulletin of the Seismological Society of America*, *69*(2), 445–450.
- 1145 Mazzotti, S., Leonard, L. J., Cassidy, J. F., Rogers, G. C., & Halchuk, S. (2011).  
 1146 Seismic hazard in western Canada from GPS strain rates versus earthquake  
 1147 catalog. *Journal of Geophysical Research: Solid Earth*, *116*(B12).
- 1148 McCaffrey, R., King, R. W., Payne, S. J., & Lancaster, M. (2013). Active tecton-  
 1149 ics of northwestern U.S. inferred from GPS-derived surface velocities. *Journal*  
 1150 *of Geophysical Research: Solid Earth*, *118*(2), 709–723.
- 1151 McCalpin, J. P., Consulting, G.-H., & Box, P. O. (1999). Criteria for Determin-  
 1152 ing the Seismic Significance of Sackungen and Other Scarplike Landforms in  
 1153 Mountainous Regions.
- 1154 Morell, K. D., Regalla, C., Amos, C. B., Bennett, S. E., Leonard, L. J., Graham, A.,  
 1155 ... Telka, A. (2018). Holocene Surface Rupture History of an Active Forearc  
 1156 Fault Redefines Seismic Hazard in Southwestern British Columbia, Canada.  
 1157 *Geophysical Research Letters*, *45*(21), 11,605–11,611.
- 1158 Morell, K. D., Regalla, C., Leonard, L. J., Amos, C. B., & Levson, V. (2017).  
 1159 Quaternary Rupture of a Crustal Fault beneath Victoria, British Columbia,  
 1160 Canada. *GSA Today*, *27*(3-4), 4–10.
- 1161 Morell, K. D., Styron, R., Stirling, M., Griffin, J., Archuleta, R., & Onur, T. (2020).

- 1162 Seismic Hazard Analyses From Geologic and Geomorphic Data: Current and  
 1163 Future Challenges. *Tectonics*, 39(10), e2018TC005365.
- 1164 Mörner, N.-A. (1991, March). Intense earthquakes and seismotectonics as a function  
 1165 of glacial isostasy. *Tectonophysics*, 188(3), 407–410.
- 1166 Mosher, D. C., & Hewitt, A. T. (2004). Late Quaternary deglaciation and sea-level  
 1167 history of eastern Juan de Fuca Strait, Cascadia. *Quaternary International*,  
 1168 121(1), 23–39.
- 1169 Muir-Wood, R. (2000, October). Deglaciation Seismotectonics: A principal in-  
 1170 fluence on intraplate seismogenesis at high latitudes. *Quaternary Science Re-  
 1171 views*, 19(14), 1399–1411.
- 1172 Muller, J. E., & Carson, D. J. T. (1969). Geology and Mineral Deposits of Alberni  
 1173 map area, British Columbia (92F). *Geological Survey of Canada Paper*.
- 1174 Nelson, A. R., Personius, S. F., Wells, R. E., Schermer, E. R., Bradley, L. A., Buck,  
 1175 J., & Reitman, N. (2017). Holocene earthquakes of magnitude 7 during  
 1176 westward escape of the Olympic Mountains, Washington. *Bulletin of the  
 1177 Seismological Society of America*, 107(5), 2394–2415.
- 1178 Personius, S. F., Briggs, R. W., Nelson, A. R., Schermer, E. R., Zebulon Maharrey,  
 1179 J., Sherrod, B. L., . . . Bradley, L. A. (2014). Holocene earthquakes and right-  
 1180 lateral slip on the left-lateral Darrington-Devils Mountain fault zone, northern  
 1181 Puget Sound, Washington. *Geosphere*, 10(6), 1482–1500.
- 1182 Personius, S. F., Dart, R. L., Bradley, L. A., & Haller, K. M. (2003). Map and data  
 1183 for Quaternary faults and folds in Oregon. *US Geological Survey Open-File Re-  
 1184 port*, 03-095, 1–550.
- 1185 Regalla, C., Fisher, D. M., Kirby, E., Oakley, D., & Taylor, S. (2017). Slip Inversion  
 1186 Along Inner Fore-Arc Faults, Eastern Tohoku, Japan. *Tectonics*, 36(11), 2647–  
 1187 2668.
- 1188 Regalla, C., Kirby, E., Mahan, S. A., McDonald, E., Pangrcic, H., Binkley, A., . . .  
 1189 Lynch, E. M. (2022). Late Holocene rupture history of the Ash Hill fault,  
 1190 Eastern California Shear Zone, and the potential for seismogenic strain trans-  
 1191 fer between nearby faults.pdf. *Earth Surface Processes and Landforms*, 47,  
 1192 2897–2925.
- 1193 Reimer, P. J., Austin, W. E., Bard, E., Bayliss, A., Blackwell, P. G., Bronk Ramsey,  
 1194 C., . . . Talamo, S. (2020). The IntCal20 Northern Hemisphere Radiocarbon

- 1195 Age Calibration Curve (0-55 cal kBP). *Radiocarbon*, 62(4), 725–757.
- 1196 Riller, U., Clark, M. D., Daxberger, H., Doman, D., Lenauer, I., Plath, S., & San-  
 1197 timano, T. (2017, August). Fault-slip inversions: Their importance in terms  
 1198 of strain, heterogeneity, and kinematics of brittle deformation. *Journal of*  
 1199 *Structural Geology*, 101, 80–95.
- 1200 Rogers, G. C. (1979, March). Earthquake fault plane solutions near Vancouver Is-  
 1201 land. *Canadian Journal of Earth Sciences*, 16(3), 523–531.
- 1202 Rogers, G. C., & Hasegawa, H. S. (1978). A second look at the British Columbia  
 1203 earthquake of June 23, 1946. *Bulletin of the Seismological Society of America*,  
 1204 68(3), 653–676.
- 1205 Ryder, J. M. (1971, February). The Stratigraphy and Morphology of Para-glacial Al-  
 1206 luvial Fans in South-central British Columbia. *Canadian Journal of Earth Sci-*  
 1207 *ences*, 8(2), 279–298.
- 1208 Scharer, K., Salisbury, J., Arrowsmith, R., & Rockwell, T. (2014, January). South-  
 1209 ern San Andreas Fault Evaluation Field Activity: Approaches to Measuring  
 1210 Small Geomorphic Offsets—Challenges and Recommendations for Active Fault  
 1211 Studies. *Seismological Research Letters*, 85, 68–76.
- 1212 Schermer, E. R., Amos, C. B., Duckworth, W. C., Nelson, A. R., Angster, S., De-  
 1213 lano, J., & Sherrod, B. L. (2021). Postglacial mw 7.0–7.5 earthquakes on the  
 1214 north olympic fault zone, Washington. *Bulletin of the Seismological Society of*  
 1215 *America*, 111(1), 490–513.
- 1216 Sherrod, B. L., Blakely, R. J., Weaver, C. S., Kelsey, H. M., Barnett, E., Liberty, L.,  
 1217 ... Pape, K. (2008). Finding concealed active faults: Extending the south-  
 1218 ern Whidbey Island fault across the Puget Lowland, Washington. *Journal of*  
 1219 *Geophysical Research: Solid Earth*, 113(5), 1–25.
- 1220 Sherrod, B. L., Brocher, T. M., Weaver, C. S., Bucknam, R. C., Blakely, R. J.,  
 1221 Kelsey, H. M., ... Haugerud, R. (2004). Holocene fault scarps near Tacoma,  
 1222 Washington, USA. *Geology*, 32(1), 9.
- 1223 Slawson, W. F., & Savage, J. C. (1979). Geodetic Deformation Associated with the  
 1224 1946 Vancouver Island, Canada, Earthquake. *Bulletin of the Seismological So-*  
 1225 *ciety of America*, 69(5), 1487–1496.
- 1226 Steffen, R., Steffen, H., Wu, P., & Eaton, D. W. (2014). Stress and fault parameters  
 1227 affecting fault slip magnitude and activation time during a glacial cycle. *Tec-*

- 1228            *tonics*, 33(7), 1461–1476.
- 1229        Stuiver, M., & Polach, H. A. (1977). Reporting of 14C data. *Radiocarbon*, 19(3),  
1230            355–363.
- 1231        Styron, R. (2019, January). The impact of earthquake cycle variability on neotec-  
1232            tonic and paleoseismic slip rate estimates. *Solid Earth*, 10(1), 15–25.
- 1233        Styron, R. H., & Sherrod, B. (2021, April). Improving Paleoseismic Earthquake  
1234            Magnitude Estimates with Rupture Length Information: Application to the  
1235            Puget Lowland, Washington State, U.S.A. *Bulletin of the Seismological Society  
1236            of America*, 111(2), 1139–1153.
- 1237        Thenhaus, P., & Campbell, K. (2002, January). Seismic hazard analysis. In *Earth-  
1238            quake Engineering Handbook* (pp. 8–1).
- 1239        van Loon, A. J. T., Pisarska-Jamroży, M., Nartišs, M., Krievāns, M., & Soms, J.  
1240            (2016, September). Seismites resulting from high-frequency, high-magnitude  
1241            earthquakes in Latvia caused by Late Glacial glacio-isostatic uplift. *Journal of  
1242            Palaeogeography*, 5(4), 363–380.
- 1243        van Wijk, J., Axen, G., & Abera, R. (2017). Initiation, evolution and extinction of  
1244            pull-apart basins: Implications for opening of the Gulf of California. *Tectono-  
1245            physics*, 719–720, 37–50.
- 1246        Van Der Woerd, J., Tapponnier, P., Ryerson, F. J., Meriaux, A.-S., Meyer, B.,  
1247            Gaudemer, Y., . . . Zhiqin, X. (2002, March). Uniform postglacial slip-rate  
1248            along the central 600 km of the Kunlun Fault (Tibet), from 26Al, 10Be, and  
1249            14C dating of riser offsets, and climatic origin of the regional morphology:  
1250            Uniform slip-rate along the Kunlun Fault. *Geophysical Journal International*,  
1251            148(3), 356–388.
- 1252        Walton, M. A., Staisch, L. M., Dura, T., Pearl, J. K., Sherrod, B., Gomberg, J., . . .  
1253            Wirth, E. (2021, May). Toward an Integrative Geological and Geophysical  
1254            View of Cascadia Subduction Zone Earthquakes. *Annual Review of Earth and  
1255            Planetary Sciences*, 49(1), 367–398.
- 1256        Wang, K. (2000). Stress-strain ‘paradox’, plate coupling, and forearc seismicity at  
1257            the Cascadia and Nankai subduction zones. *Tectonophysics*, 319(4), 321–338.
- 1258        Wang, K., Mulder, T., Rogers, G., & Hyndman, R. (1995, July). Case for very low  
1259            coupling stress on the Cascadia Ssubduction Fault. *Journal of Geophysical Re-  
1260            search*, 100.

- 1261 Wells, D. L., & Coppersmith, K. J. (1994). Empirical relationships among magni-  
1262 tude, rupture length, rupture width, rupture area and surface displacements.  
1263 *Bulletin of the Seismological Society of America*, *84*(4), 974–1002.
- 1264 Wells, R. E., Blakely, R. J., & Bemis, S. (2020). Northward migration of the Oregon  
1265 forearc on the Gales Creek fault. *Geosphere*, *16*(2), 660–684.
- 1266 Wells, R. E., Weaver, C. S., & Blakely, R. J. (1998). Fore-arc migration in Cascadia  
1267 and its neotectonic significance. *Geology*, *26*(8), 759–762.
- 1268 Wesnousky, S. G. (2008, August). Displacement and Geometrical Characteristics  
1269 of Earthquake Surface Ruptures: Issues and Implications for Seismic-Hazard  
1270 Analysis and the Process of Earthquake Rupture. *Bulletin of the Seismological*  
1271 *Society of America*, *98*(4), 1609–1632.
- 1272 Yorath, C. J., Clowes, R. M., Green, A. G., Sutherland-Brown, A., Brandon, M. T.,  
1273 Massey, N. W., . . . Hyndman, R. D. (1985). Lithoprobe - Phase 1: Southern  
1274 Vancouver Island: Preliminary Analyses of Reflection Seismic Profiles and Sur-  
1275 face Geological Studies. *Paper - Geological Survey of Canada*(pt A), 543–554.
- 1276 Yorath, C. J., Green, A. G., Clowes, R. M., Brown, A. S., Brandon, M. T.,  
1277 Kanasewich, E. R., & Spencer, C. (1985). Lithoprobe , southern Vancou-  
1278 ver Island: Seismic reflection sees through Wrangellia to the Juan de Fuca  
1279 plate. *Geology*, *13*(13), 759–762.
- 1280 Zinke, R., Dolan, J. F., Rhodes, E. J., Van Dissen, R., & McGuire, C. P. (2017).  
1281 Highly Variable Latest Pleistocene-Holocene Incremental Slip Rates on the  
1282 Awatere Fault at Saxton River, South Island, New Zealand, Revealed by Lidar  
1283 Mapping and Luminescence Dating. *Geophysical Research Letters*, *44*(22),  
1284 11,301–11,310.